Shock and Vibration

# Seismic-Resilient Disaster Prevention of Engineering Systems Based on Dynamic Soil-Structure Interaction

Lead Guest Editor: Yu Huang
Guest Editors: Chun-xiang Li, Zhi-Yi Chen, Chongqiang Zhu, and Liyuan Cao

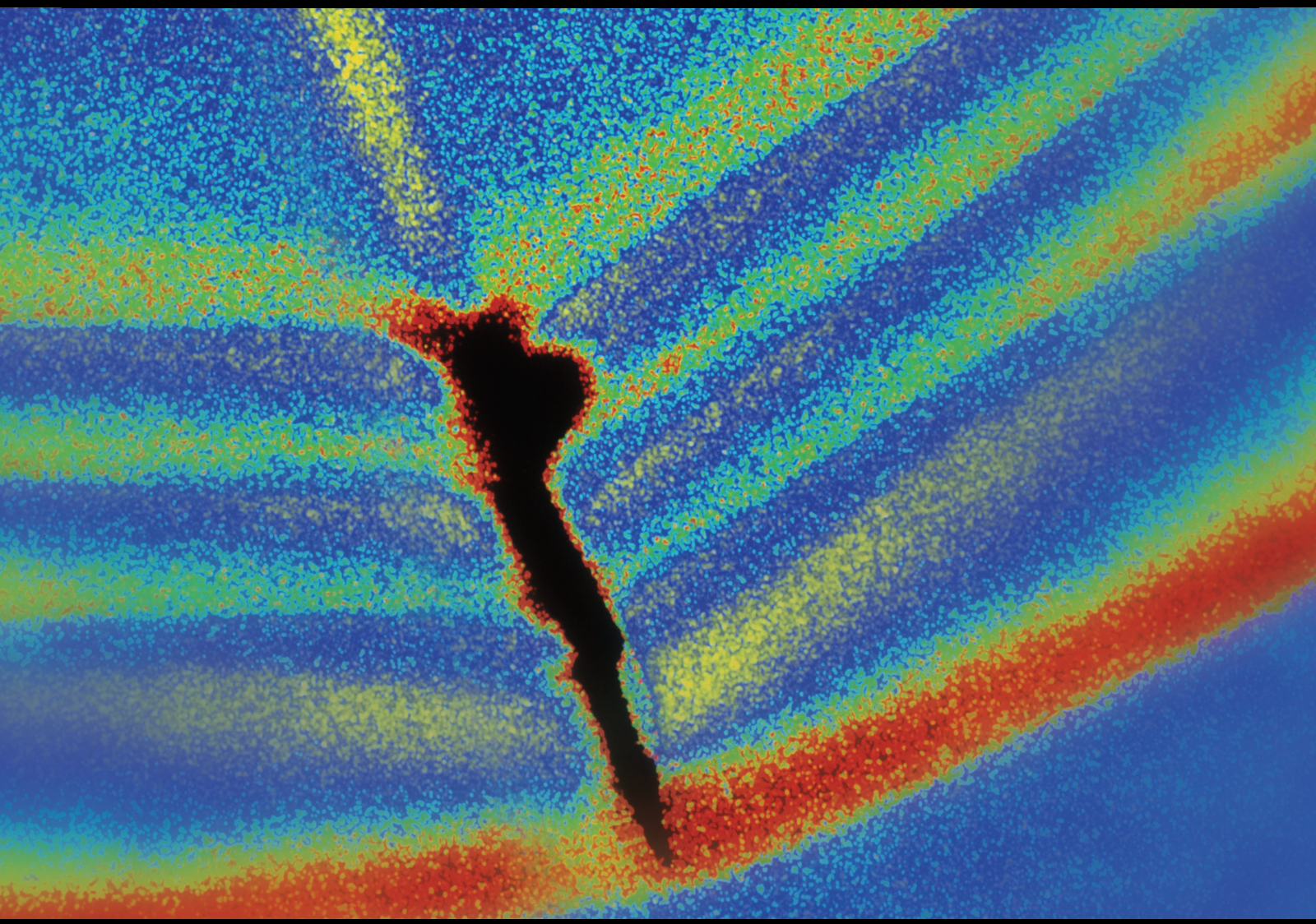

# Seismic-Resilient Disaster Prevention of Engineering Systems Based on Dynamic Soil-Structure Interaction

Shock and Vibration

# Seismic-Resilient Disaster Prevention of Engineering Systems Based on Dynamic Soil-Structure Interaction

Lead Guest Editor: Yu Huang
Guest Editors: Chun-xiang Li, Zhi-Yi Chen, Chongqiang Zhu, and Liyuan Cao

Copyright © 2022 Hindawi Limited. All rights reserved.

This is a special issue published in “Shock and Vibration.” All articles are open access articles distributed under the Creative Commons Attribution License, which permits unrestricted use, distribution, and reproduction in any medium, provided the original work is properly cited.

# Chief Editor

Huu-Tai Thai, Australia

## Associate Editors

Ivo Caliò, Italy
Nawawi Chouw, New Zealand
Longjun Dong, China
Farzad Ebrahimi, Iran
Mickaël Lallart, France
Vadim V. Silberschmidt, United Kingdom
Mario Terzo, Italy
Angelo Marcelo Tusset, Brazil

## Academic Editors

Omid A. Yamini, Iran
Maher Abdelghani, Tunisia
Haim Abramovich, Israel
Desmond Adair, Kazakhstan
Manuel Aenlle Lopez, Spain
Brij N. Agrawal, USA
Ehsan Ahmadi, United Kingdom
Felix Albu, Romania
Marco Alfano, Italy
Sara Amoroso, Italy
Huaming An, China
P. Antonaci, Italy
José V. Araújo dos Santos, Portugal
Lutz Auersch, Germany
Matteo Aureli, USA
Azwan I. Azmi, Malaysia
Antonio Batista, Brazil
Mattia Battarra, Italy
Marco Belloli, Italy
Francisco Beltran-Carbajal, Mexico
Denis Benasciutti, Italy
Marta Berardengo, Italy
Sébastien Besset, France
Giosuè Boscato, Italy
Fabio Botta, Italy
Giuseppe Brandonisio, Italy
Francesco Bucchi, Italy
Rafał Burdzik, Poland
Salvatore Caddemi, Italy
Wahyu Caesarendra, Brunei Darussalam
Baoping Cai, China
Sandro Carbonari, Italy
Cristina Castejón, Spain
Nicola Caterino, Italy
Gabriele Cazzulani, Italy
Athanasios Chasalevris, Greece
Guoda Chen, China
Xavier Chiementin, France
Simone Cinquemani, Italy
Marco Civera, Italy
Marco Cocconcelli, Italy
Alvaro Cunha, Portugal
Giorgio Dalpiaz, Italy
Thanh-Phong Dao, Vietnam
Arka Jyoti Das, India
Raj Das, Australia
Silvio L.T. De Souza, Brazil
Xiaowei Deng, Hong Kong
Dario Di Maio, The Netherlands
Raffaella Di Sante, Italy
Luigi Di Sarno, Italy
Enrique Lopez Droguett, Chile
Mădălina Dumitriu, Romania
Sami El-Borgi, Qatar
Mohammad Elahinia, USA
Said Elias, Iceland
Selçuk Erkaya, Turkey
Gaoliang Fang, Canada
Fiorenzo A. Fazzolari, United Kingdom
Luis A. Felipe-Sese, Spain
Matteo Filippi, Italy
Piotr Folęga, Poland
Paola Forte, Italy
Francesco Franco, Italy
Juan C. G. Prada, Spain
Roman Gabl, United Kingdom
Pedro Galvín, Spain
Jinqiang Gan, China
Cong Gao, China
Arturo García Garcia-Perez, Mexico
Rozaimi Ghazali, Malaysia
Marco Gherlone, Italy
Anindya Ghoshal, USA
Gilbert R. Gillich, Romania
Antonio Giuffrida, Italy
Annalisa Greco, Italy
Jiajie Guo, China

Amal Hajjaj, United Kingdom
Mohammad A. Hariri-Ardebili, USA
Seyed M. Hashemi, Canada
Xue-qiu He, China
Agustin Herrera-May, Mexico
M.I. Herreros, Spain
Duc-Duy Ho, Vietnam
Hamid Hosano, Japan
Jin Huang, China
Ahmed Ibrahim, USA
Bernard W. Ikua, Kenya
Xingxing Jiang, China
Jiang Jin, China
Xiaohang Jin, China
MOUSTAFA KASSEM, Malaysia
Shao-Bo Kang, China
Yuri S. Karinski, Israel
Andrzej Katunin, Poland
Manoj Khandelwal, Australia
Denise-Penelope Kontoni, Greece
Mohammadreza Koopialipoor, Iran
Georges Kouroussis, Belgium
Genadijus Kulvietis, Lithuania
Pradeep Kundu, USA
Luca Landi, Italy
Moon G. Lee, Republic of Korea
Trupti Ranjan Lenka, India
Arcanjo Lenzi, Brazil
Marco Lepidi, Italy
Jinhua Li, China
Shuang Li, China
Zhixiong Li, China
Xihui Liang, Canada
Tzu-Kang Lin, Taiwan
Jinxin Liu, China
Ruonan Liu, China
Xiuquan Liu, China
Siliang Lu, China
Yixiang Lu, China
R. Luo, China
Tianshou Ma, China
Nuno M. Maia, Portugal
Abdollah Malekjafarian, Ireland
Stefano Manzoni, Italy
Stefano Marchesiello, Italy
Francesco S. Marulo, Italy
Traian Mazilu, Romania
Vittorio Memmolo, Italy
Jean-Mathieu Mencik, France
Laurent Mevel, France
Letícia Fleck Fadel Miguel, Brazil
FuRen Ming, China
Fabio Minghini, Italy
Marco Miniaci, USA
Mahdi Mohammadpour, United Kingdom
Rui Moreira, Portugal
Emiliano Mucchi, Italy
Peter Múčka, Slovakia
Fehmi Najar, Tunisia
M. Z. Naser, USA
Amr A. Nassr, Egypt
Sundararajan Natarajan, India
Toshiaki Natsuki, Japan
Miguel Neves, Portugal
Sy Dzung Nguyen, Republic of Korea
Trung Nguyen-Thoi, Vietnam
Gianni Niccolini, Italy
Rodrigo Nicoletti, Brazil
Bin Niu, China
Leilei Niu, China
Yan Niu, China
Lucio Olivares, Italy
Erkan Oterkus, United Kingdom
Roberto Palma, Spain
Junhong Park, Republic of Korea
Francesco Pellicano, Italy
Paolo Pennacchi, Italy
Giuseppe Petrone, Italy
Evgeny Petrov, United Kingdom
Franck Poisson, France
Luca Pugi, Italy
Yi Qin, China
Virginio Quaglini, Italy
Mohammad Rafiee, Canada
Carlo Rainieri, Italy
Vasudevan Rajamohan, India
Ricardo A. Ramirez-Mendoza, Mexico
José J. Rangel-Magdaleno, Mexico

Didier Rémond, France
Dario Richiedei, Italy
Fabio Rizzo, Italy
Carlo Rosso, Italy
Riccardo Rubini, Italy
Salvatore Russo, Italy
Giuseppe Ruta, Italy
Edoardo Sabbioni, Italy
Pouyan Roodgar Saffari, Iran
Filippo Santucci de Magistris, Italy
Fabrizio Scozzese, Italy
Abdullah Seçgin, Turkey
Roger Serra, France
S. Mahdi Seyed-Kolbadi, Iran
Yujie Shen, China
Bao-Jun Shi, China
Chengzhi Shi, USA
Gerardo Silva-Navarro, Mexico
Marcos Silveira, Brazil
Kumar V. Singh, USA
Jean-Jacques Sinou, France
Isabelle Sochet, France
Alba Sofi, Italy
Jussi Sopanen, Finland
Stefano Sorace, Italy
Andrea Spaggiari, Italy
Lei Su, China
Shuaishuai Sun, Australia
Fidelis Tawiah Suorineni, Kazakhstan
Cecilia Surace, Italy
Tomasz Szolc, Poland
Iacopo Tamellin, Italy
Zhuhua Tan, China
Gang Tang, China
Chao Tao, China
Tianyou Tao, China
Marco Tarabini, Italy
Hamid Toopchi-Nezhad, Iran
Carlo Trigona, Italy
Federica Tubino, Italy
Nerio Tullini, Italy
Nicolò Vaiana, Italy
Marcello Vanali, Italy
Christian Vanhille, Spain
Dr. Govind Vashishtha, Poland
F. Viadero, Spain
M. Ahmer Wadee, United Kingdom
C. M. Wang, Australia
Gaoxin Wang, China
Huiqi Wang, China
Pengfei Wang, China
Weiqiang Wang, Australia
Xian-Bo Wang, China
YuRen Wang, China
Wai-on Wong, Hong Kong
Yuanping XU, China
Biao Xiang, China
Qilong Xue, China
Xin Xue, China
Diansen Yang, China
Jie Yang, Australia
Chang-Ping Yi, Sweden
Nicolo Zampieri, Italy
Chao-Ping Zang, China
Enrico Zappino, Italy
Guo-Qing Zhang, China
Shaojian Zhang, China
Yongfang Zhang, China
Yaobing Zhao, China
Zhipeng Zhao, Japan
Changjie Zheng, China
Chuanbo Zhou, China
Hongwei Zhou, China
Hongyuan Zhou, China
Jiaxi Zhou, China
Yunlai Zhou, China
Radoslaw Zimroz, Poland

# Contents

Hindawi
Shock and Vibration
Volume 2022, Article ID 1517406, 16 pages
https://doi.org/10.1155/2022/1517406

*Research Article*

# Investigation of Small-Scaled Soil Structure Model under Earthquake Loads via Small Shaking Table Tests

**Mohammed El Hoseny**,[1,2] **Jianxun Ma**,[1] **Dong Luo**,[1] **and Yanchao Yue**[1]

[1]*School of Human Settlements and Civil Engineering, Xi'an Jiaotong University, Xi'an 710054, Shaanxi Province, China*
[2]*Faculty of Engineering at Shoubra, Benha University, Cairo 11629, Egypt*

Correspondence should be addressed to Mohammed El Hoseny; mohammed.elhoseny@stu.xjtu.edu.cn and Jianxun Ma; majx@mail.xjtu.edu.cn

Received 4 July 2022; Revised 16 August 2022; Accepted 29 August 2022; Published 26 September 2022

Academic Editor: Chongqiang Zhu

Copyright © 2022 Mohammed El Hoseny et al. This is an open access article distributed under the Creative Commons Attribution License, which permits unrestricted use, distribution, and reproduction in any medium, provided the original work is properly cited.

This paper aims to determine the appropriate scaling coefficient rigorously in the dynamic analysis of structures via small shaking table tests to represent the full real case while considering the soil-structure interaction problem. In addition, we investigate the seismic effects of the superstructure with flexible and fixed bases. To achieve this purpose, seven stories of concrete moment-resisting frames supported on silty clay soil were scaled. According to the shaking table specifications, a small-scaled soil-structure model was executed with a scaled factor of 1 : 50. Consequently, the scale steel skeleton model was built to represent the real superstructure. In addition, the laminar soil container for the soil block was constructed to reduce undesirable boundary effects. Three earthquakes have been applied at the superstructure base as a fixed base and at the bottom of the soil block in the soil structure system as a flexible base. The numerical simulations are implemented for scaled and real models. According to obtained results from experimental and numerical investigations, the numerical model achieved good results with experimental observation. In addition, the small scaling factor of 1 : 50 can represent the seismic response of full construction conditions with acceptable precision. It is observed that the flexible base has overestimated in lateral displacement of the real superstructure compared with a fixed base, in which the maximum amplification percentage at the roof floor level reaches up to 98% under seismic load. Otherwise, the shear force distribution along the height and base shear of the superstructure with a flexible base decreases compared with a fixed base. The maximum reduction percentage is 38% under seismic load. Consequently, the safety and cost of the superstructure are affected.

## 1. Introduction

Most civil designer engineers consider the structure's support a fixed base during seismic analysis and design. This assumption is improper because there is an interaction effect between the soil and structure during seismic motions, especially in the presence of weak soil. Therefore, it is imperative to investigate the effects of soil-structure interaction on lateral displacements, shear force distributions of different column locations, and base shear of the superstructure under seismic loads. The significance of the dynamic soil-structure interaction (SSI) is summarized into two components: the inertial component and the kinematic component. Both components are generally affected by the seismic structural response [1, 2]. Most of the researchers focus on analytical [3–5] and numerical studies [6–9] more than on experimental investigations [10, 11]. Pioneering work was proposed to develop the hybrid numerical method (finite element method, moving particle simulation) to simulate the complex dynamic behavior of structures [12]. The developed numerical method was verified with a series of benchmark problems, whether they were analytical or experimental studies. Other studies [13, 14] performed a full simulation of the centrifuge model using the three-dimensional (3D) discrete-element method (DEM). This model was validated with other physical experimental results to check its effectiveness and accuracy. While in this study [15], they performed large-scale shaking table tests to

investigate the near-fault ground motions effects on the seismic response of slopes. They mainly depended on experimental results. Consequently, numerical and analytical studies without experimental observations may not be convincing in practical engineering. In turn, the validated numerical analyses provide an alternative to experimental observations. Therefore, carrying out a shaking table test considering the SSI effect combined with the corresponding numerical simulation is preferable. Such as in Reference [16], the researchers evaluated the seismic response of reinforced concrete structures by using smart materials along with plastic hinges of the beams to resist the high strain under cyclic and seismic loads. The numerical analyses were performed by the seismo struct model and verified the results with other laboratory reports. The experimental and numerical results were in good agreement. However, this study neglected the effects of SSI under seismic loads. In addition, another study [17] performed a three-dimensional finite element analysis by ANSIS software on a Structure-Soil Structure Interaction (SSSI) test. The numerical model was verified with experimental results to carry out many parametric studies with practical applications in engineering. The large-scale modeling at 1 : 15 was applied to two buildings with 12-story cast-in-place concrete frames. To reduce the undesirable boundary effects, the soil container was flexible and cylindrical. By comparing the results of numerical simulations with experimental observations, the built modeling is suitable for numerical simulation analyses with other parametric studies. Moreover, in Reference [18], large-scale shaking table tests with a scale factor of 1 : 4 on a six-story steel frame structure supported on a pile group with SSI effects and on a rigid foundation were performed. The numerical simulation method using ABAQUS software was validated with experimental results. It is concluded that the SSI effects have become more considerable. A series of shaking table tests and theoretical analyses on liquefiable soils in pile group foundations of tall buildings were studied to evaluate the seismic responses of structure, foundation, and soil under major, moderate, and minor earthquakes [19]. They analyzed the results derived from the shaking table tests, including a free-field test, a structure on a rigid foundation test, and a long pile-soil structure. The scaling coefficient applied in this study was 1 : 10 for a concrete structure cast in place with a 12-story. The seismic responses of a structure with pile SSI are affected and compared with a rigid foundation case. The same researchers [20] performed on 12-story concrete moment resisting frames supported on pile foundations on soft soil and fixed bases to study the dynamic effects of SSI under seismic loads. Large-scale shaking table tests with a scaling coefficient of 1 : 6 were applied. A shear laminar container was used to minimize the effects of soil boundaries during experiments. The results showed that the effects of SSI have been amplified in lateral displacements and inter-story drifts compared with no SSI effects. In contrast, the inter-story shear force decreases with SSI compared with a fixed base. While reference [21] investigated reinforced concrete buildings with fourteen stories as full-scale in the Republic of Srpska under different seismic motions. Other researchers [22] applied a full-scale soil-structure simple frame with cross bracings. Most of the mentioned studies with full-scale and large-scale factors are better and more concise. However, such research execution would be difficult due to skilled labor requirements, high-technical instruments, consumption of more time, and high cost.

A few researchers [23, 24] provided other methods to represent the full real soil-structure model via small shaking table capacity with low cost to assess the seismic structure response considering the SSI effects. To achieve this type of research, the derived data from laboratory measurements are compared with numerical simulations to check the accuracy of the results [25]. Consequently, the novelties of this research are to verify adequate accuracy for the appropriate small scaling coefficient of the coupled soil structure system via small shaking table tests under seismic loads. In addition, investigate the seismic response of the superstructure without SSI and with SSI effects. To achieve these issues, a series of experimental studies were performed on a small shaking table at the American University in Cairo (AUC), Egypt. The dimensions of the small shaking table are a width of 1.30 m and a length of 1.70 m. In addition, the maximum carry-over load is five tones.

## 2. Methodology

*2.1. Real Soil-Structure Model System.* The real superstructure consists of seven concrete moment-resisting frames with a raft foundation. The total height of the building is 21 m and consists of double bays in both directions. Each direction with a bay span is 4.0 m. The soil layer is silty clay with a unit weight of $\gamma = 17.8\,\text{kN/m}^3$ and a shear wave velocity of 220 m/s. Also, the soil block's length, width, and depth are 70 m, 50 m, and 40 m, respectively. The configuration of the real soil-structure model and sectional plan with concrete dimensions is displayed in Figure 1.

A numerical investigation was carried out by SAP2000 software [26] of a real superstructure with a fixed base, as displayed in Figure 2, to check the safety and adequate section properties. Afterward, conclude the fundamental period of the superstructure and total mass as depicted in Table 1.

*2.2. Scaled Soil Structure Model System.* To achieve the accuracy measurement from the laboratory tests with the real model, the appropriate geometric scaling coefficient has been determined according to shaking table specifications (dimensions and characteristics). The scaling model is geometric scaling and kinematic or dynamic scaling. Many works of literature verified and checked the geometric and dynamic similitude laws of scaled models with real models [27, 28] and had good agreement results. Therefore, the Cauchy condition presented the similitude laws of the geometric and dynamic scaled models used in shaking table tests [29]. Table 2 shows the similitude laws of geometric and dynamic scaling factors.

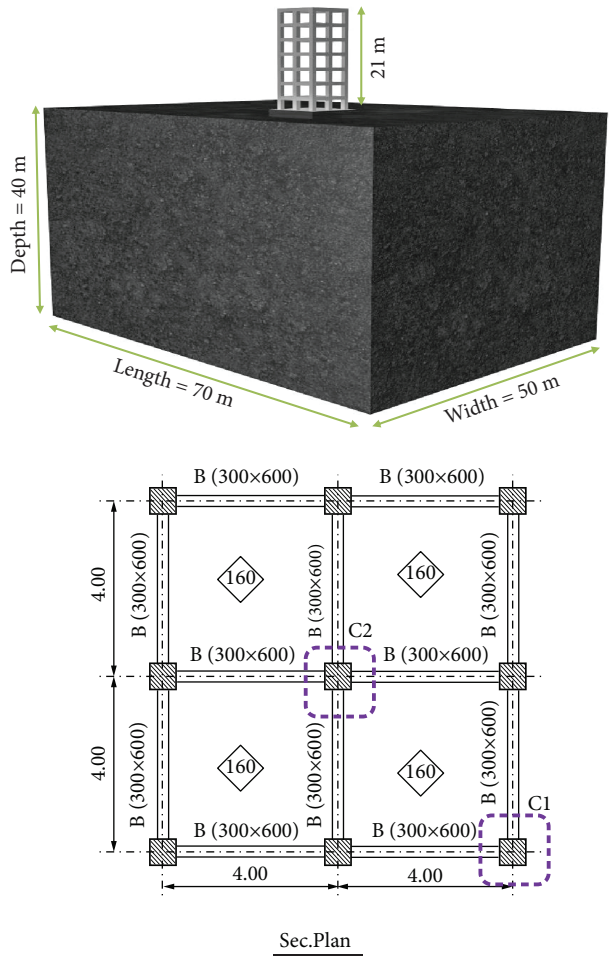


Figure 1: Configuration of real soil-structure model.

According to the small shaking table specifications, the appropriate scaling coefficient was chosen to be $\lambda = 1:50$. Therefore, the total height of the scaled superstructure was 0.42 m, and the width in both directions was 0.16 m. The equivalent steel-scaled model was used as an alternate solution to represent the concrete moment resisting frames due to the volume and weight of the concrete. In addition, the length, width, and depth of the soil layer were scaled to be 1.4 m, 1.0 m, and 0.8 m, respectively. For the superstructure, to conclude the time period and total mass of the steel skeleton structure, the real model's time period and total mass in Table 1 should be scaled according to the similitude laws displayed in Table 2. The scaled factor of a time period and mass are $\lambda^{0.5}$ and $\lambda^{3}$, respectively. Therefore, Table 3 shows the required time period and mass of the scaled superstructure with a fixed base.

A numerical model was built by SAP2000 to conclude the section properties of the steel skeleton to achieve the properties in Table 3. The trial and error method was applied to reach the properties of the steel skeleton structure. Figure 3 presents the final dimensions and section properties of the steel skeleton model with a mild steel grade of 240/350, in which all connections between elements were welded. As a result, the adopted time period and total mass of the superstructure are shown in Table 4. It is noted that the maximum difference between the adopted and required properties of the superstructure does not exceed 1.9% in the mass item. Consequently, the scaled model was manufactured in the workshop.

*2.2.1. Scaled Soil Properties.* The soil layer cannot be placed directly on the shaking table. Therefore, many researchers [30, 31] described a laminar soil container to represent the soil boundary and maintain the soil layer as a real condition. According to similarity rules, the scaled geotechnical model's length, width, and depth were 1.40 m, 1.00 m, and 0.80 m, respectively. The material components of the laminar shear box consisted of aluminum and rubber layers that were joined by a high-strength resin material. The use of aluminum material is due to possessing ductile properties and low weight [32, 33]. In addition, the wood plate was fixed at the level of the shaking table.

To conclude the dimensions of the aluminum and rubber sections, the natural frequency of the laminar shear box is matched with the natural frequency of the soil block to prevent any waves from an interface between container and soil during seismic excitations, which was determined as 9.43 Hz. Therefore, the laminar shear box was manufactured in the workshop, as shown in Figure 4. The soil properties used in this research are shown in Table 5 [28].

*2.3. Earthquake Records.* Three seismic displacement time histories with different frequency contents, such as Kobe (1995), Northridge (1994), and Chi-Chi (1999) earthquakes, are applied at the bottom of the soil in the soil structure model system and the base of the superstructure in the fixed base case. Scaled displacement time histories were concluded according to similitude laws in Table 2. Therefore, real and scaled displacement time histories are displayed in Figures 5–7, in addition to the characteristics of the real earthquakes [34].

## 3. Experimental Investigations

*3.1. Seismic Response of Scaled Structure Model without and with SSI Effects.* Firstly, it is essential to check the time period of the scaled superstructure without SSI effects (fixed base) that matched with numerical analyses before being exposed to seismic motions. Therefore, the scaled structure was put on the shaking table and fixed with four bolts with a diameter of 16 mm (4M16). The LVDT (Linear Variable Differential Transformer) was set up at the roof floor level to measure the response of the superstructure (as shown in Figure 8). A sine sweep test was implemented to check the scaled model's time period. The first resonance between the shaking table and the scaled model indicated the scale model's time period.

Consequently, the time period of the scaled superstructure with a fixed base was 0.0869 seconds, which matched with the numerical analysis in Table 4. Afterward, three different scaled earthquakes were applied at the base of the structure. The lateral displacement obtained from the experimental investigation at the roof floor level was an absolute lateral displacement that represented the displacement of the shaking table (earthquake motion) plus the

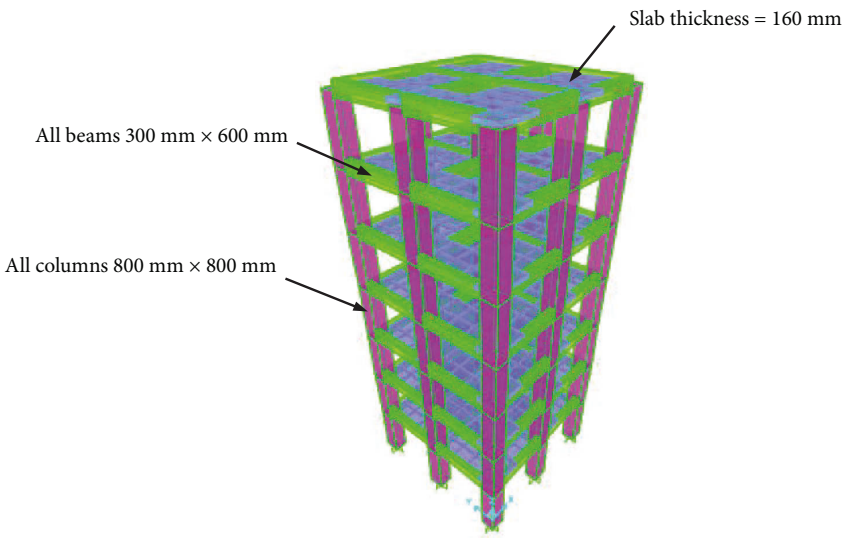


Figure 2: Real superstructure with fixed base by SAP2000 software.

Table 1: Time period and total mass of the superstructure with a fixed base.

| | |
|---|---|
| Time period (second) | 0.617 |
| Total masses (tones) | 645 |

Table 2: Similitude laws of the geometric and dynamic scaling factor.

| | |
|---|---|
| Mass density | 1 |
| Stiffness | $\lambda^{2}$ |
| Force | $\lambda^{3}$ |
| Modulus | $\lambda$ |
| Strain | 1 |
| Time | $\lambda^{0.5}$ |
| Shear wave velocity | $\lambda^{0.5}$ |
| Frequency | $\lambda^{-0.5}$ |
| Acceleration | 1 |
| Stress | $\lambda$ |
| Length | $\lambda$ |
| Mass | $\lambda^{3}$ |

Table 3: Required time period and total mass of the scaled superstructure with a fixed base.

| | |
|---|---|
| Time period (second) | 0.087 |
| Total masses (Kg) | 5.16 |

relative displacement of the superstructure (distortion displacement).

For the SSI case, the laminar soil container was placed on the shaking table and fixed by 14M16 after placing the soil layer. Afterward, the scaled structure was placed in the determined place in the middle of the soil. Finally, LVDT was placed at the roof floor level as in the fixed base case. Figure 9 depicts the scaled soil-structure system in the laboratory. Before applying the three scaled earthquakes, a sine sweep test was performed at the resonance frequency at the shaking table to obtain the scaled model's time period. Therefore, the time period of the superstructure with a flexible base was approximately 0.095 seconds.

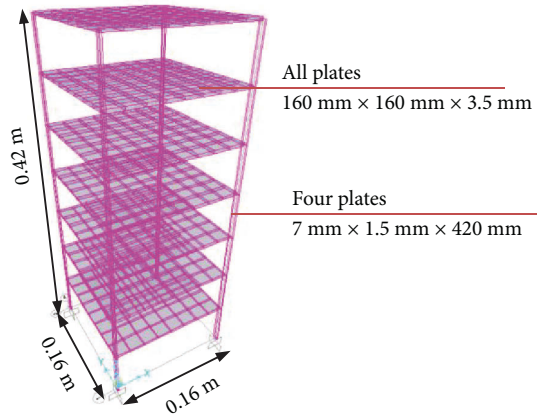


Figure 3: Dimension and section properties of steel skeleton.

Table 4: Adopted time period and total mass of the scaled superstructure with a fixed base.

| | |
|---|---|
| Time period (second) | 0.086 |
| Total masses (Kg) | 5.06 |

It is observed that the flexible base has been amplified in the time period by 9.3% in comparison with the fixed base case.

Three scaled seismic waves were applied at the base of the soil block level. The absolute lateral displacements were produced at roof floor level, including the movement of the input motion, a rocking component due to foundation rotation, and a relative lateral displacement of the superstructure (distortion component).

## 4. Numerical Approaches

*4.1. Seismic Response of Real and Scaled Structure Models without and with SSI Effects.* Numerical analyses were carried out to verify the experimental investigation. In addition, simulate other parametric studies to evaluate the SSI effects compared with a fixed base. By referring to the real and

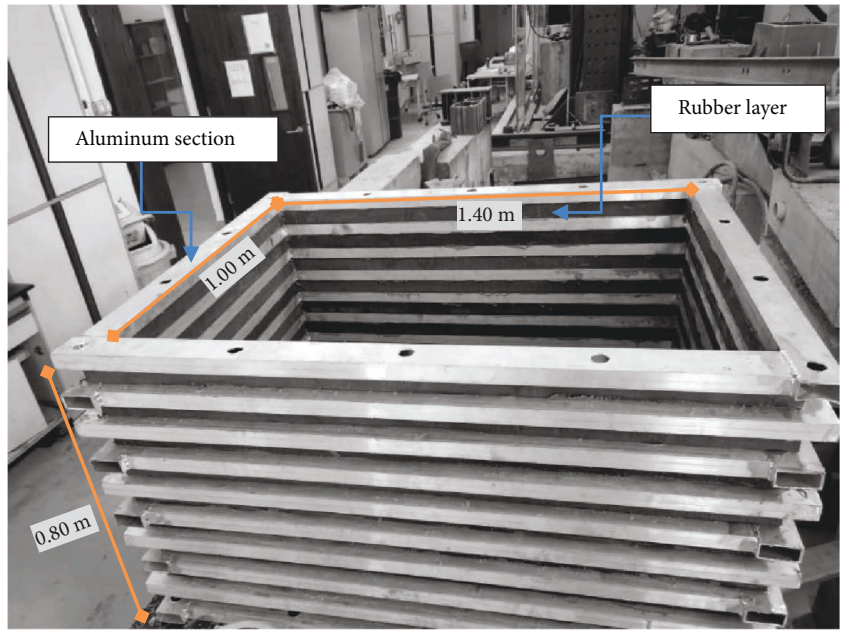


Figure 4: Laminar shear box.

Table 5: Soil properties for scaled SSI system.

| Parameter | Symbol | Magnitude | Unit |
|---|---|---|---|
| Average unit weight | $\gamma$ | 17.8 | kN/m$^3$ |
| Young modulus | $E$ | 4571 | kN/m$^2$ |
| Shear modulus | $G$ | 1758 | kN/m$^2$ |
| Compression wave velocity | $V_p$ | 58.23 | m/s |
| Shear wave velocity | $V_s$ | 31.13 | m/s |
| Poisson's ratio | $\nu$ | 0.3 | — |
| Cohesion | $c$ | 60 | kN/m$^2$ |
| Dilatancy angle | $\psi$ | 1.8 | (degree) |
| Friction angle | ø | 31.8 | (degree) |

scaled numerical models with fixed bases in Sections 2.1 and 2.2, three seismic motions were applied at the fixed bases of the superstructure. Therefore, the absolute lateral displacements at each floor level for real and scaled models were obtained.

For the SSI case, 3D numerical models with a flexible base were built by PLAXIS 3D software [35] for real and scaled models. The direct method was applied, considering the soil and structure during seismic motions in one step. This model consisted of structural elements, soil blocks, the interface between soil and structure elements, boundary conditions, and input motion. The structure elements consist of slab elements as plate elements and beams and columns as beam elements with the mentioned properties in Sections 2.1 and 2.2. In addition, the soil modeling in this study was the Mohr–Coulomb (MC) criteria (linear-elastic perfectly plastic), for which many researchers [10, 28] had good results for this model. The soil layer properties of the scaled model system are given in Table 5. By applying the similitude laws in Table 2, the properties of the real soil layer are concluded. The interface model properties between soil and structure elements are the same as soil blocks with a reduction factor of 0.67, as mentioned in the PLAXIS manual [35]. The appropriate boundaries were set up in the soil block, in which the soil in the natural case is infinity in all lateral directions. Therefore, free field boundaries with damping dashpots were applied to the lateral boundaries of the soil block to absorb any reflecting seismic waves. The base of the soil block was assumed to be the bedrock base where earthquake loads were employed, as in Figure 10. Therefore, after applying three seismic motions at the bottom of the soil block, the absolute lateral displacements at each floor level under three seismic scenarios for real and scaled models were investigated.

## 5. Results and Discussion

*5.1. Verification of Experimental and Numerical Simulation.* Firstly, in this section, the scaled model's numerical analyses and experimental investigations are verified in terms of maximum absolute lateral displacement under different frequency contents

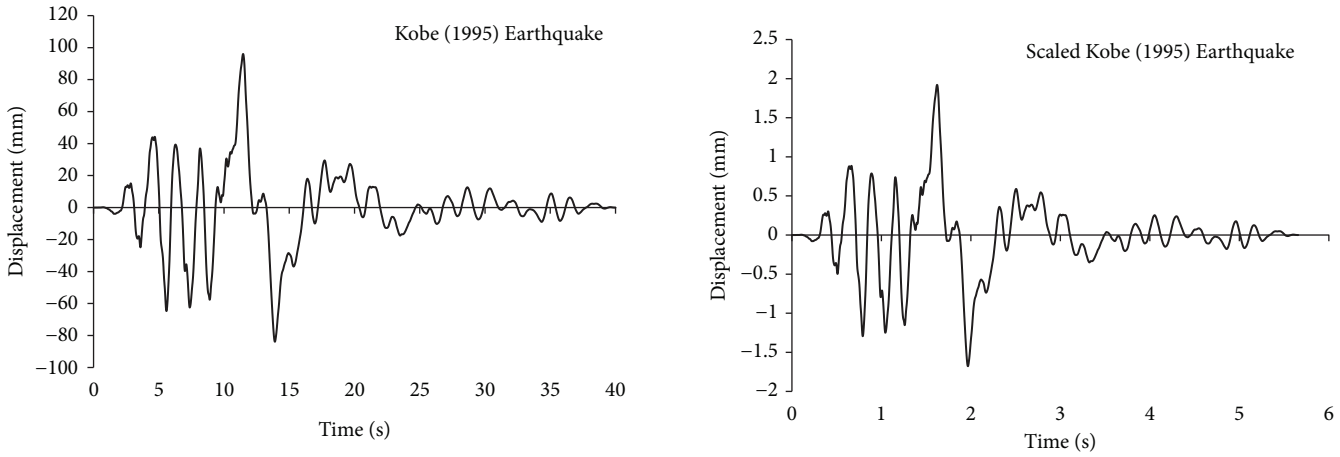


| Earthquake | Country | Date | PGA (g) | Mw (R) | Duration (s) | Station |
|---|---|---|---|---|---|---|
| Kobe | Japan | Jan.1995 | 0.34 | 6.9 | 40 | KAKOGAWA |

Figure 5: Original and scaled Kobe (1995) earthquake.

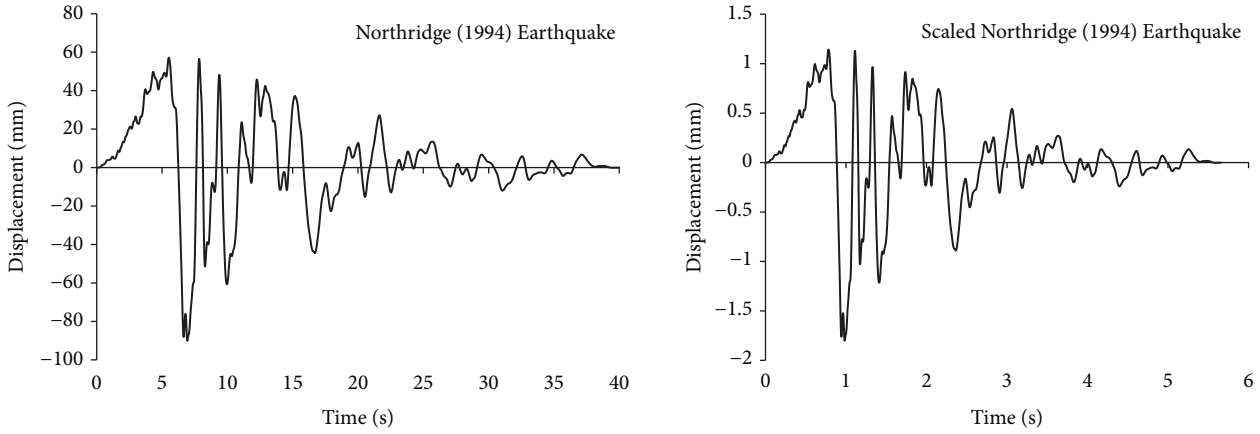


| Earthquake | Country | Date | PGA (g) | Mw (R) | Duration (s) | Station |
|---|---|---|---|---|---|---|
| Northridge | USA | Jan.1994 | 0.57 | 6.7 | 40 | CDMG STATION 24278 |

Figure 6: Original and scaled Northridge (1994) earthquake.

of earthquakes. Therefore, Figures 11 and 12 display the maximum absolute lateral displacements along the height derived from numerical analyses with experimental results at the roof floor level under scaled earthquakes for fixed and flexible bases, respectively. It is noted that the experimental and numerical results at roof level are adequate and achieve high accuracy. The maximum deviation between experimental and numerical results at the roof level is 4% in both conditions: fixed and flexible bases.

After ensuring that the experimental and numerical results of the scaled model were in very good agreement with high accuracy, the second phase in the verification is to check the appropriate scaling coefficient, achieving good results in the dynamic analyses. To perform this process, the maximum absolute lateral displacement of the real model is divided by the maximum absolute lateral displacement of the scaled model at each floor level of the superstructure under three seismic motions for each case: fixed and flexible bases. Figure 13 displays the maximum absolute lateral displacements of the real model derived from numerical analyses at each floor level with fixed and flexible bases that showed the effects of SSI compared with the fixed base case. By performing the division process, Figures 14(a) and 14(b) exhibit the resulting inverse scaling coefficients ($1/\lambda$) along the height of the superstructure under

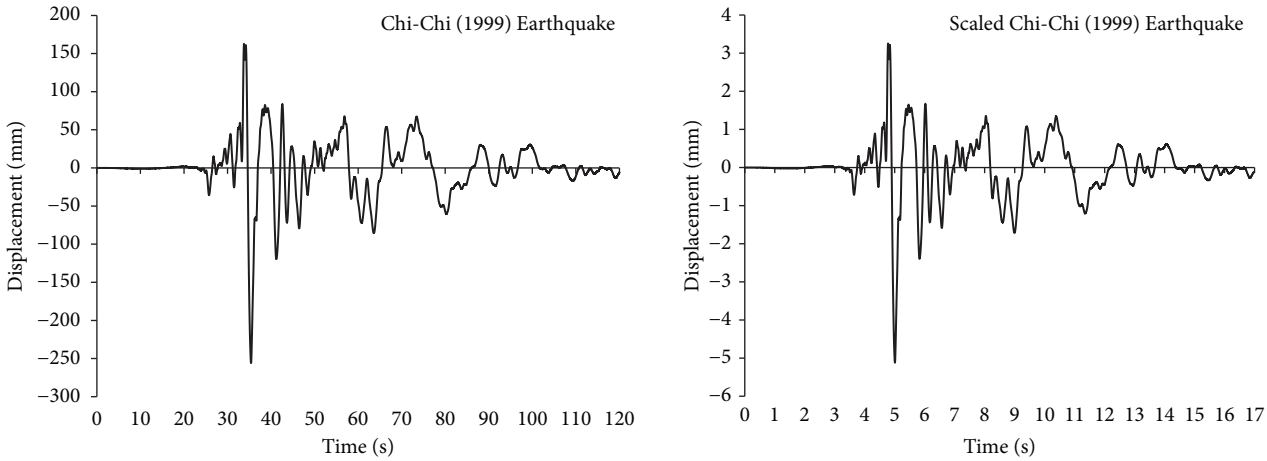


| Earthquake | Country | Date | PGA (g) | Mw (R) | Duration (s) | Station |
|---|---|---|---|---|---|---|
| Chi-Chi | Taiwan | Sep.1999 | 0.36 | 7.6 | 120 | CHY006 |

Figure 7: Original and scaled Chi-Chi (1999) earthquake.

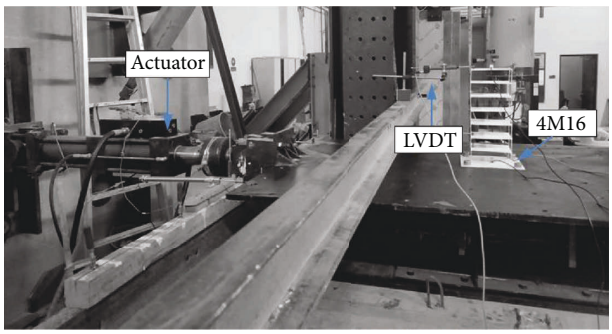


Figure 8: Scaled structure fixation on shaking table and LVDT installation.

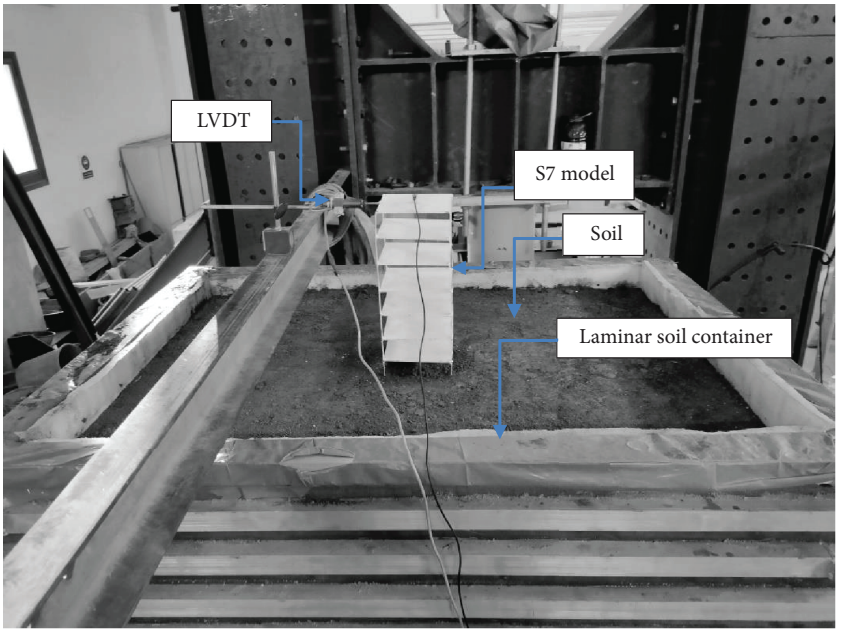


Figure 9: Scaled soil-structure interaction system.

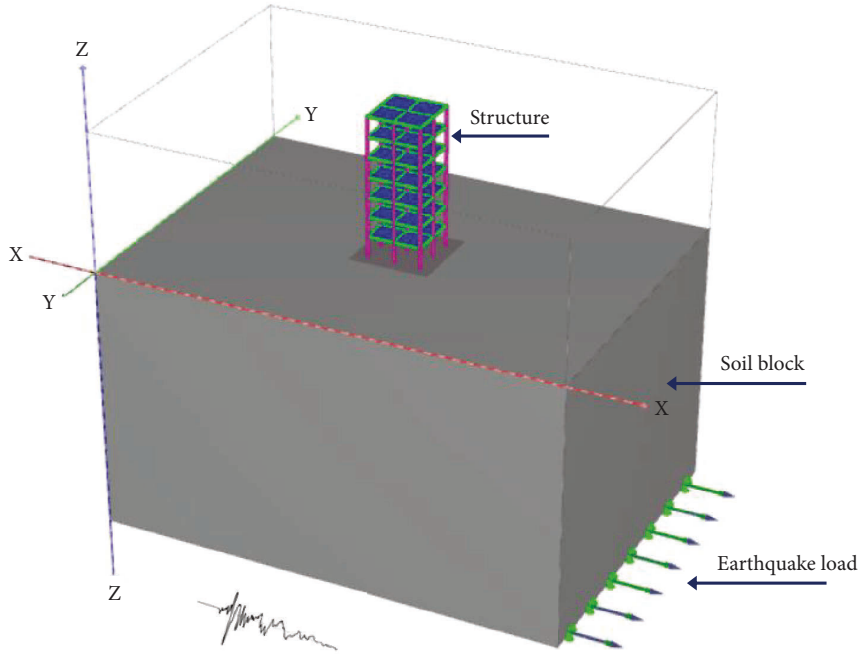


Figure 10: Soil structure interaction model by PLAXIS.

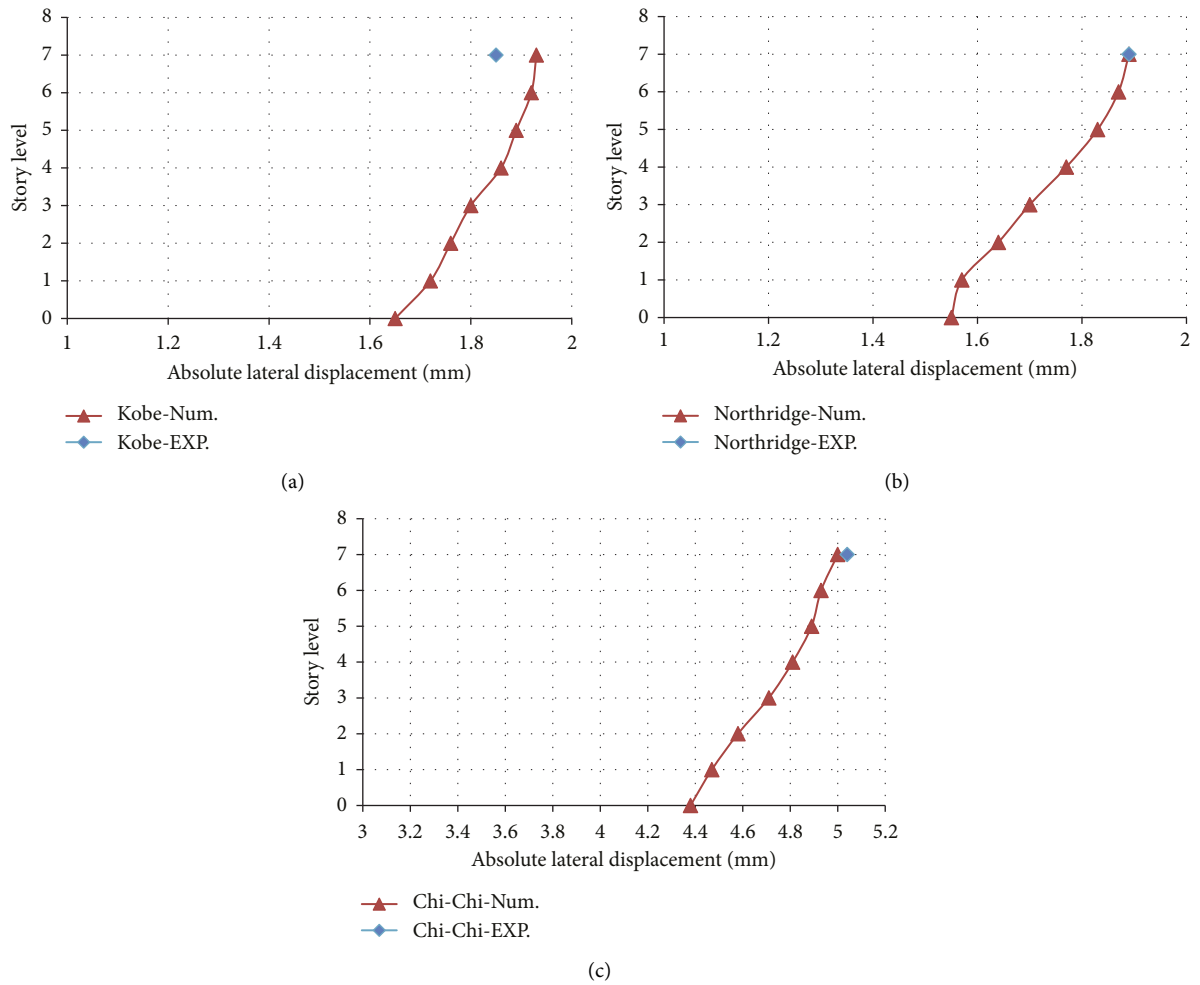


Figure 11: Maximum absolute lateral displacements derived numerically and experimentally in a fixed base case under three scaled earthquakes: (a) Kobe. (b) Northridge. (c) Chi-Chi.

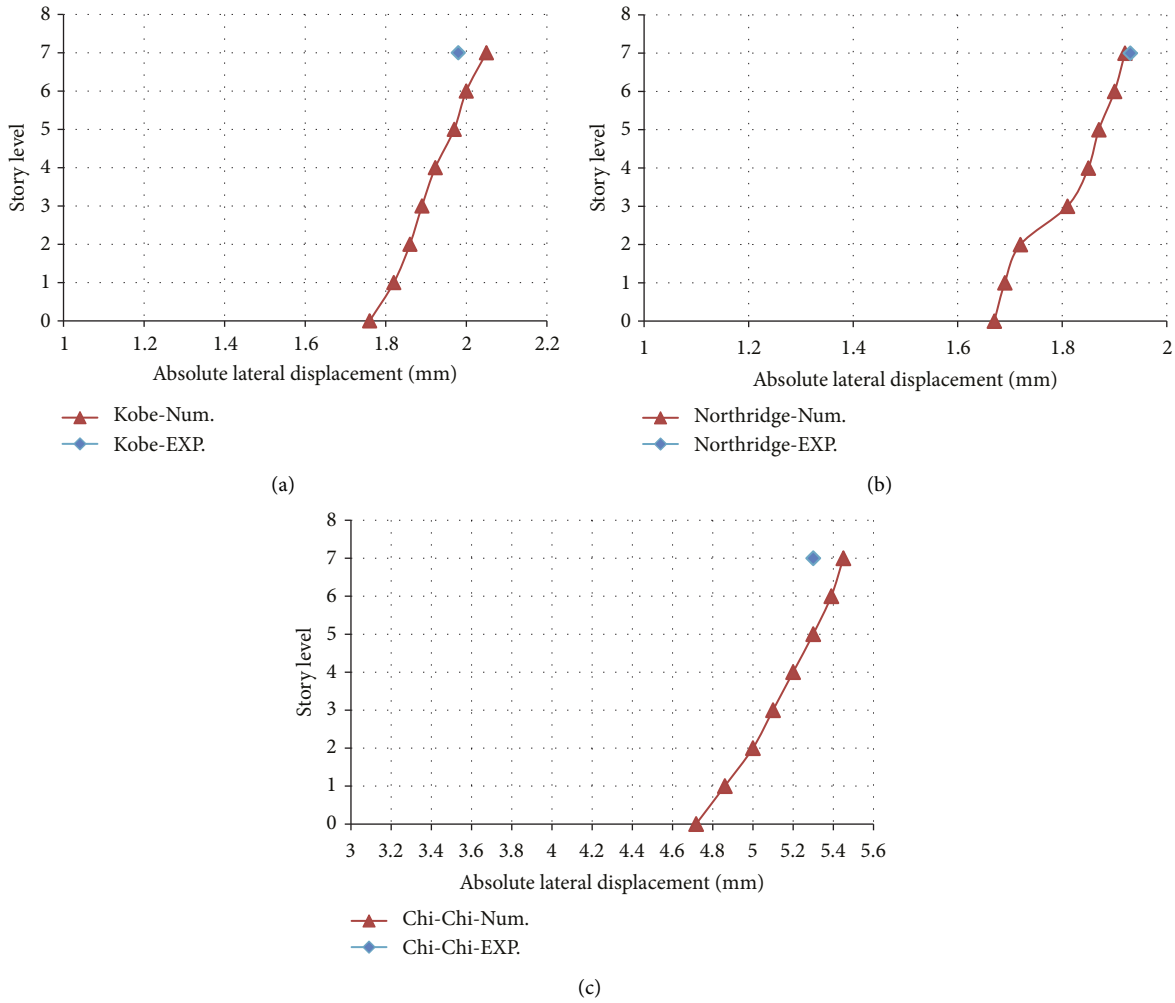


Figure 12: Maximum absolute lateral displacements derived numerically and experimentally in a flexible base case under three scaled earthquakes: (a) Kobe. (b) Northridge. (c) Chi-Chi.

three earthquakes for fixed and flexible bases cases, respectively. The target scaling coefficient used in this study was 1 : 50. Therefore, it is observed that the maximum scaling coefficient is 1 : 58 in a fixed base case under the Chi-Chi and Kobe earthquakes that occurred at the foundation level. While under the Northridge earthquake, the maximum scaling coefficient is 1 : 61 at the roof floor level. Consequently, the selected scaling factor of 1 : 50 achieves adequate accuracy under three seismic motions along the height of the superstructure with a fixed base. In the flexible base case, the maximum scaling coefficient along the height of the superstructure is 1 : 59 under Chi-Chi and Kobe earthquakes that occurred at the foundation level. While under the Northridge earthquake, the values of the scaling coefficient are considered good results from the foundation level to the fourth level (less than 1 : 60). However, the maximum scaling coefficient under the Northridge earthquake is 1 : 67 at the roof floor level.

Generally, the selected scaling coefficient of 1 : 50 is regarded as a suitable scaling factor in the seismic analysis to represent the full-scale real construction model under different seismic scenarios.

*5.2. Relative Lateral Displacements of the Superstructure.* After ensuring the adequacy of the numerical model, it is suitable to study other parametric to investigate the seismic response of a real superstructure with flexible and fixed bases under different seismic scenarios. The previous results derived from experimental and numerical investigations were absolute lateral displacement that included the movement of the earthquake, relative lateral displacement of the structure (distortion component) that was different in flexible about fixed bases, and a rocking component due to foundation rotation in the flexible base case only. Because the movement of the earthquake is the conjoint movement in both fixed and flexible bases, the displacement time histories at each floor level will be subtracted from the displacement time histories of earthquakes. For example, Figures 15 and 16 show the absolute displacement time histories at the roof floor level with different seismic motions and the resulted relative displacement after subtraction at each time step for fixed and flexible bases, respectively. The resulting relative displacement time histories may be in phase, out-

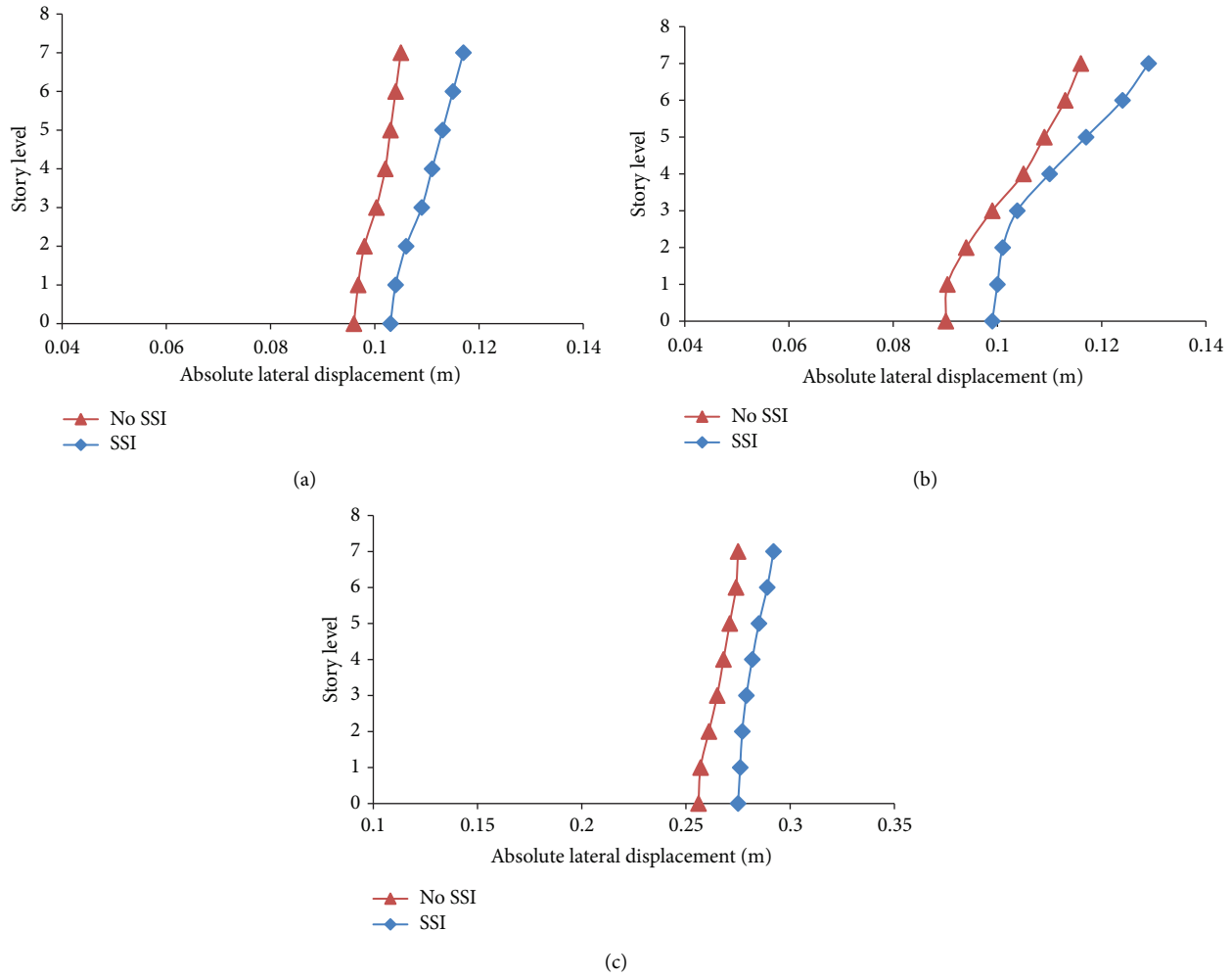


Figure 13: Maximum absolute lateral displacement at each floor level with flexible and fixed bases under three real earthquakes: (a) Kobe. (b) Northridge. (c) Chi-Chi.

of-phase, the same sign, or different from absolute and seismic motion time histories.

Consequently, the relative lateral displacement is considered to study the effects of SSI and is compared with a fixed base. Figures 17 displays the maximum relative lateral displacement at each floor level of the real superstructure with fixed and flexible cases under different earthquakes. It is observed that the flexible base has amplified lateral displacement at the roof floor level by 98% under Kobe, 74% under Northridge, and 58% under the Chi-Chi earthquakes. Therefore, the fixed base is unsuitable to represent the structures support under seismic loads, and the fixed base assumption is underestimated in lateral displacement. Consequently, the safety of the superstructure is affected.

*5.3. Shear Force Distribution and Base Shear of the Superstructure.* The shear force distribution and base shear are important to analyze and design the structural elements of the superstructure due to earthquake loads. Therefore, Figures 18 and 19 display the maximum envelope shear force distribution along the height of external and internal columns of the superstructure with different support conditions under three seismic loads, respectively. For the external column (C1), it is noted that the flexible base has reduced shear force distribution along the height of the superstructure compared with a fixed base case. The reduction percentages at the base level are 19%, 9%, and 38% under the Kobe, Northridge, and Chi-Chi earthquakes, respectively. While for the internal column (C2), the shear force distribution for the fixed base at the first-floor level to the foundation level is different compared with the flexible base. It may be referred to as its support condition and position. Generally, it is also noted that the flexible base has a reduced shear force distribution along the height compared with the fixed base case. The reduction percentages at the foundation level are 1%, 5%, and 26% under the Kobe, Northridge, and Chi-Chi earthquakes, respectively.

Finally, Figure 20 presents the maximum envelope base shear force for the superstructure under three seismic loads with flexible and fixed bases. It is noted that the flexible base has reduced base shear compared with a

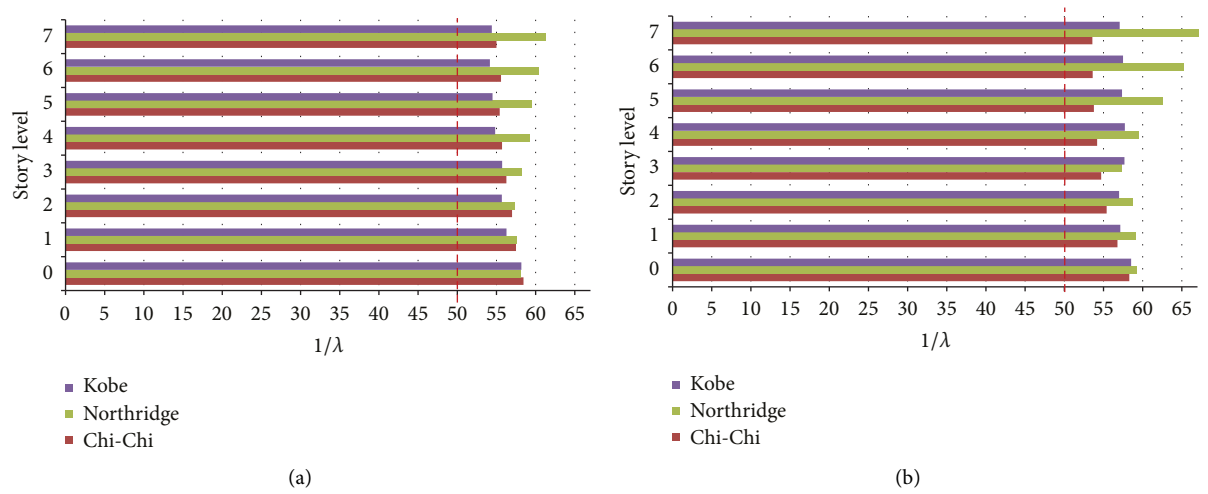


FIGURE 14: Resulting the inverse scaling coefficients ($1/\lambda$) at each floor level of the superstructure under three earthquakes in the cases: (a) fixed base, (b) flexible base.

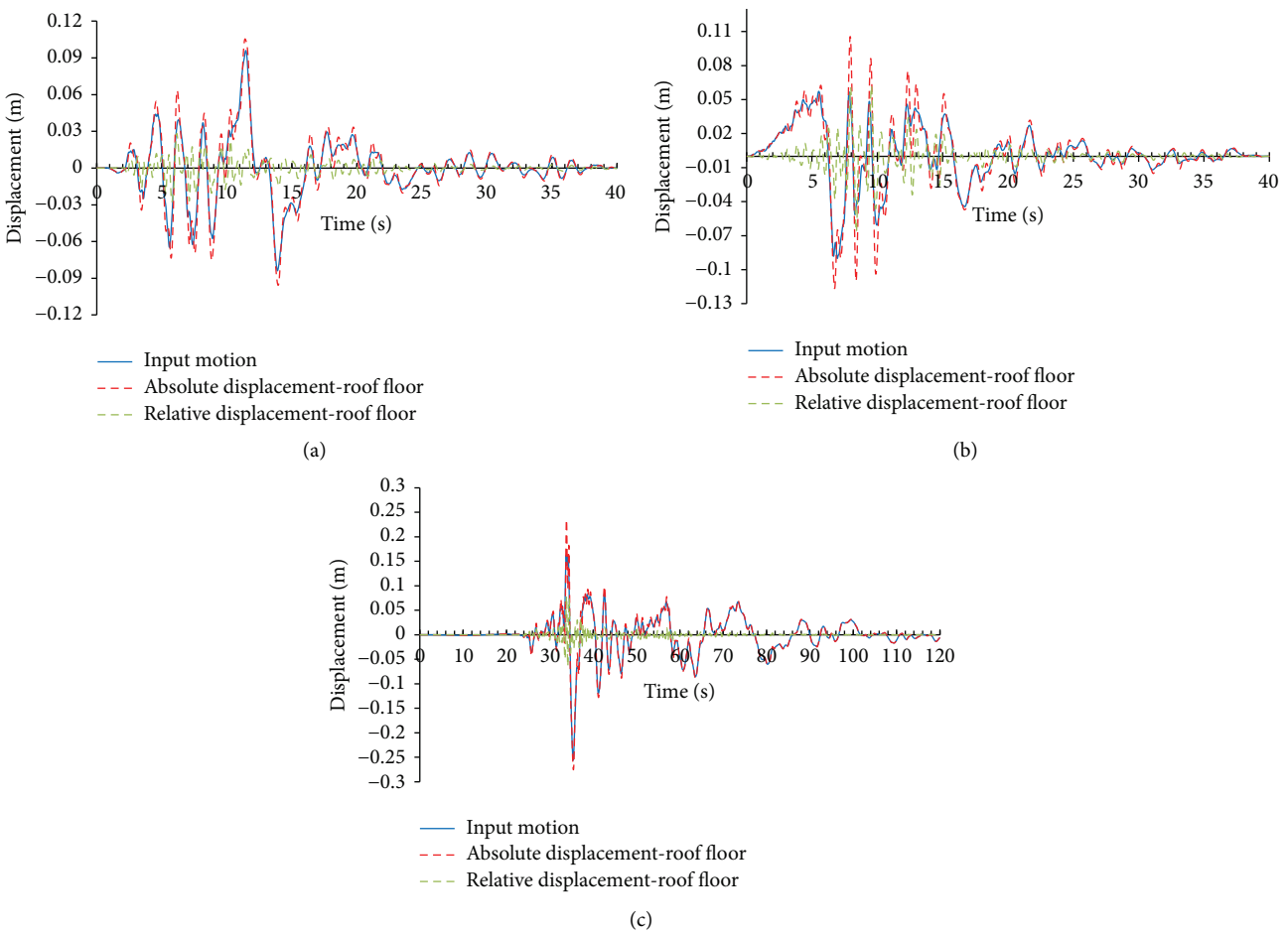


FIGURE 15: Lateral displacement time histories at the roof floor and the superstructure base (input motion) with a fixed base under three real earthquakes: (a) Kobe. (b) Northridge. (c) Chi-Chi.

fixed base under different seismic loads. The reduction percentages are 2%, 12.5%, and 37.5% under the Kobe, Northridge, and Chi-Chi earthquakes, respectively. Consequently, the fixed base is considered improper to represent the structure's support under seismic scenarios, and the fixed base assumption is overestimated in shear force distribution and base shear force. Therefore, the cost of the superstructure is affected.

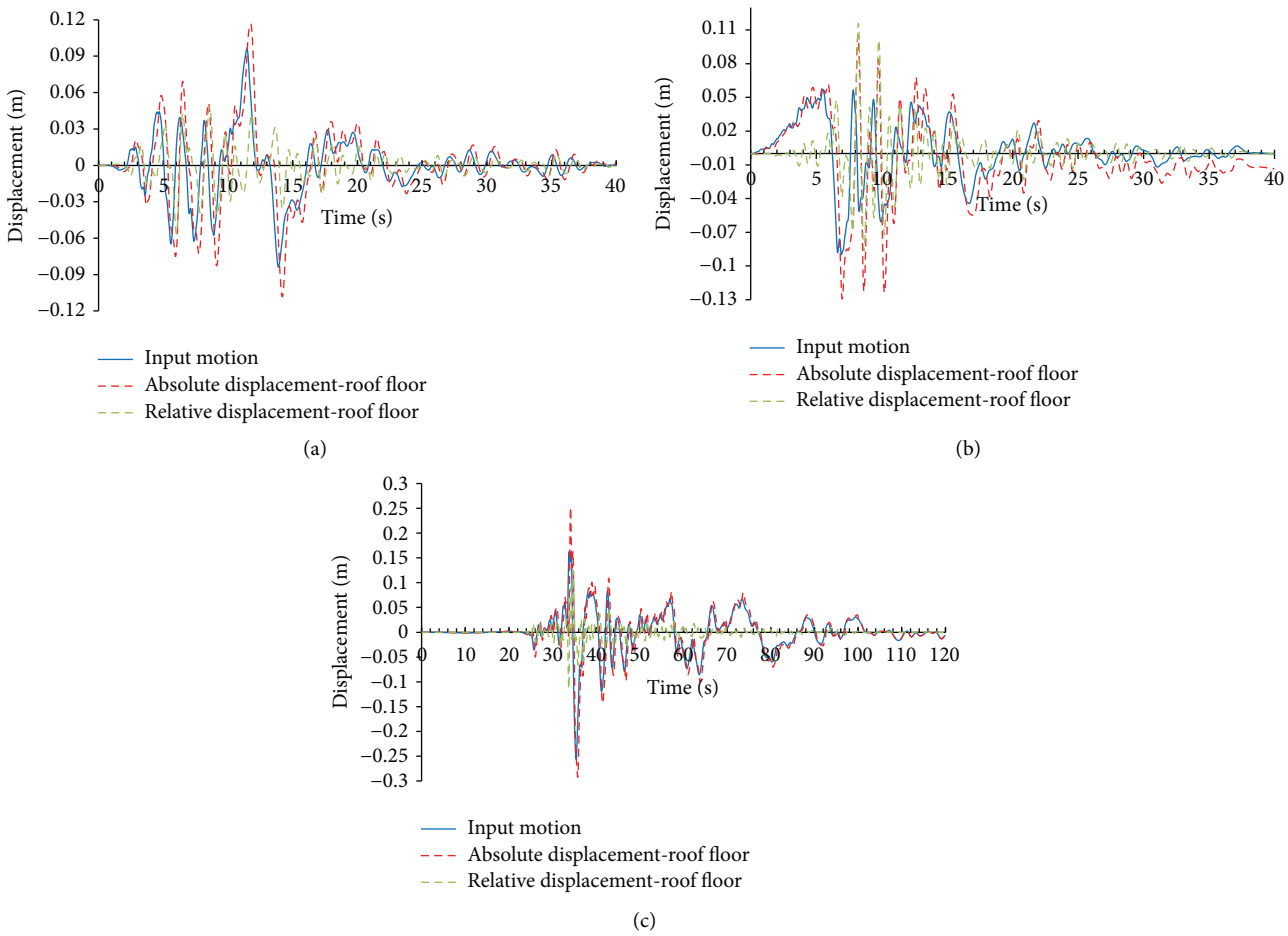


Figure 16: Lateral displacement time histories at the roof floor level and the soil block base (input motion) with flexible base under three real earthquakes: (a) Kobe. (b) Northridge. (c) Chi-Chi.

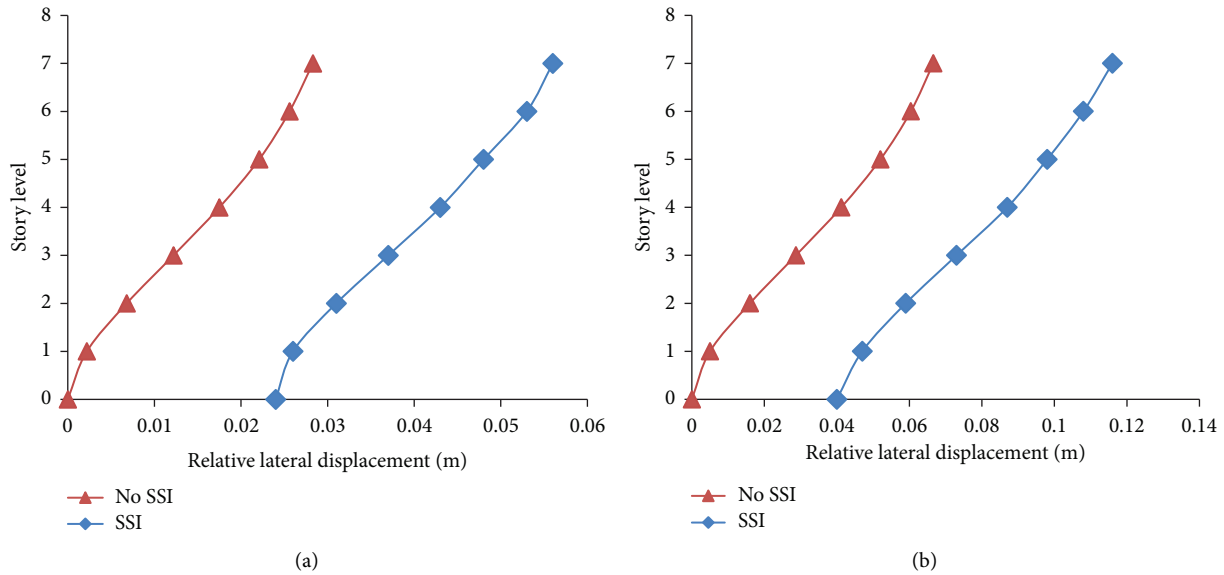


Figure 17: Continued.

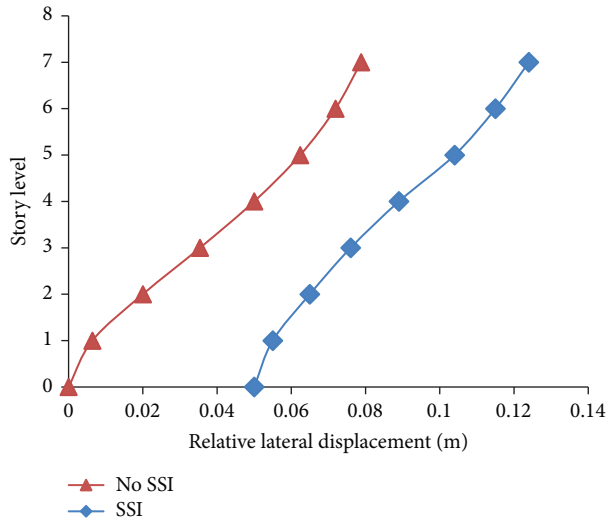


(c)

Figure 17: Maximum relative lateral displacements at each floor level of the real superstructure without and with SSI effects under three earthquakes (a) Kobe. (b) Northridge. (c) Chi-Chi.

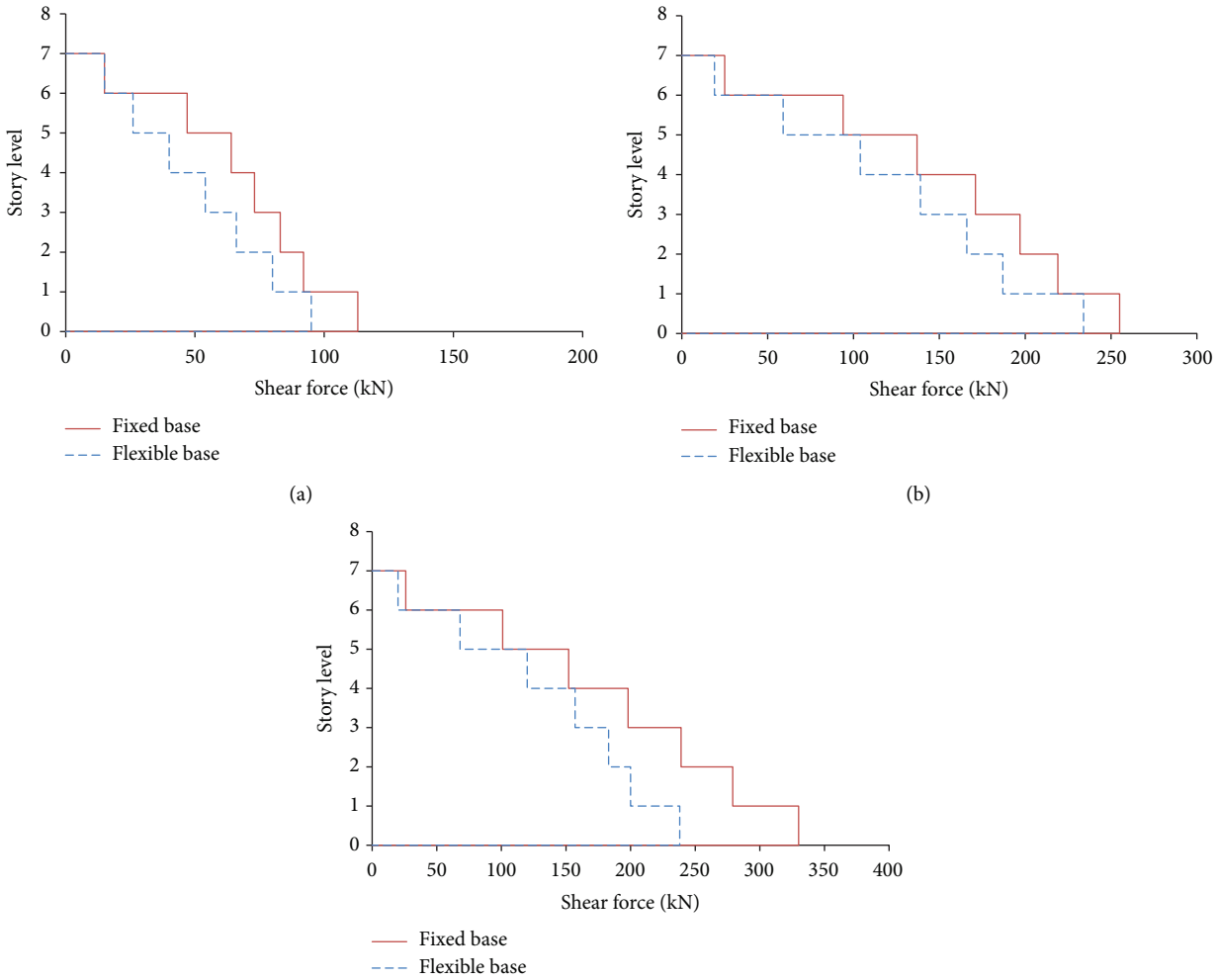


(a)

(b)

(c)

Figure 18: Maximum envelope shear force distribution of external column (C1) at the corner along the height for superstructure with flexible and fixed bases under three earthquakes: (a) Kobe. (b) Northridge. (c) Chi-Chi.

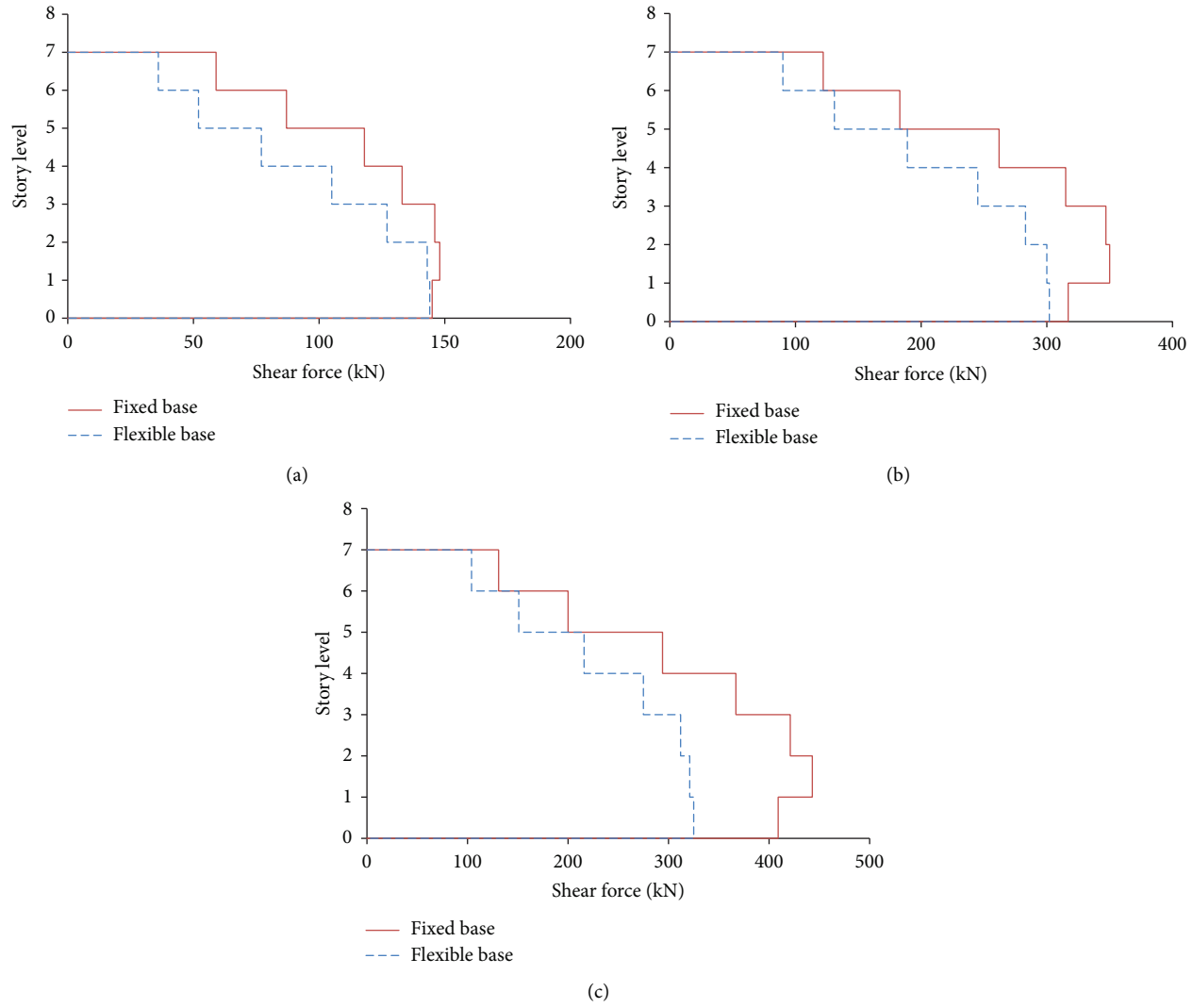


Figure 19: Maximum envelope shear force distribution of internal column (C2) at the internal along the height for superstructure with flexible and fixed bases under three earthquakes: (a) Kobe. (b) Northridge. (c) Chi-Chi.

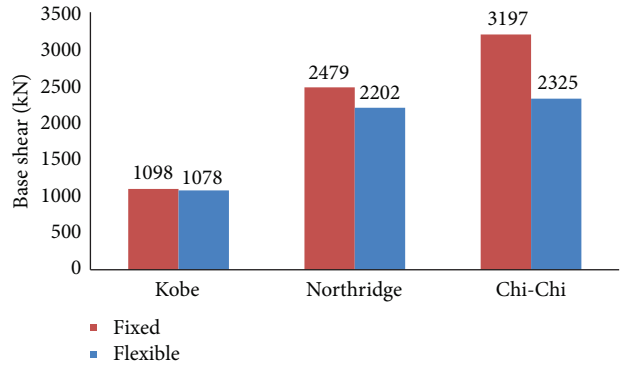


Figure 20: Maximum envelope base shear force at the base of the superstructure with flexible and fixed bases under three earthquakes.

## 6. Conclusions

This paper uses experimental observations and numerical simulations to study the soil structure model on a small shaking table under seismic loads. In addition, investigate the seismic response of the superstructure with flexible and fixed bases. Seven stories of concrete moment-resisting frames rested on silty clay soil with a shear wave

velocity of 220 m/s were scaled. The scale coefficient applied in this study was 1 : 50, according to the specifications of the shaking table. Consequently, a steel-scaled structure model was manufactured. In addition, a laminar soil container was implemented to decrease undesirable boundary effects. The seismic loads were applied at the base of the superstructure with a fixed base and at the bottom of the soil block in the flexible base case. The numerical simulations were verified with experimental investigations to ensure the adequacy of the numerical model. Afterward, verified the adequacy of the appropriate scaling coefficient in the seismic analyses. Finally, the seismic behavior of the real model with fixed and flexible bases was discussed in terms of relative lateral displacement, shear force distributions for external and internal columns, and base shear of the superstructure under different seismic loads.

The results derived from the numerical analysis of the scaled model were very accurate with experimental measurements under three scaled seismic motions. In addition, the selected scaling coefficient of 1 : 50 achieved accepted accuracy in the dynamic analysis under different frequency contents. It is observed that the flexible base had amplified lateral displacement compared with the fixed base. Subsequently, the fixed base assumption was underestimated in lateral displacement compared with soil deposits. Consequently, the safety of the superstructure is affected. Otherwise, the flexible base reduced the shear force distribution of external and internal columns and the base shear of the superstructure compared with the fixed base. Therefore, the fixed base assumption was overestimated in the shear force distribution and base shear of the superstructure. Consequently, the cost is affected.

## Data Availability

The data used to support the findings of this study are available from the corresponding author upon request.

## Conflicts of Interest

The authors declare that they have no conflicts of interest regarding the publication of this paper.

## Acknowledgments

This work was supported by the construction laboratory at the American University in Cairo (AUC), Egypt, and Omar El Kadi, the authors thank them for supporting them in this laboratory. This research was funded by the National Natural Science Foundation of China (NSFC), grant no. 51178390.

## References

[1] J. Lysmer, T. Udaka, C. Tsai, and H. B. Seed, *FLUSH-A Computer Program for Approximate 3-D Analysis of Soil-Structure Interaction Problems*, California Univ, California, CA, U.S.A, 1975.

[2] J. P. Stewart, R. B. Seed, and G. L. Fenves, *Empirical Evaluation of Inertial Soil-Structure Interaction Effects*, Pacific Earthquake Engineering Research Center Univ. of California, Berkeley, CA, U.S.A, 1998.

[3] M. Novak and Y. O. Beredugo, "Vertical Vibration of Embedded Footings," *Journal Of the Soil Mechanics And Foundations Division*, vol. 98, pp. 1291–1310, 1972.

[4] R. J. Apsel and J. E. Luco, "Torsional response of rigid embedded foundation," *Journal of the Engineering Mechanics Division*, vol. 102, no. 6, pp. 957–970, 1976.

[5] H. U. Kim, J. G. Ha, K. W. Ko, and D. S. Kim, "Optimization of Two Soil-Structure Interaction Parameters Using Dynamic Centrifuge Tests and an Analytical Approach," *Sustainability*, vol. 12, 2020.

[6] R. Scarfone, M. Morigi, and R. Conti, "Assessment of Dynamic Soil-Structure Interaction Effects for Tall Buildings: A 3D Numerical Approach," *Soil Dynamics And Earthquake Engineering*, vol. 128, Article ID 105864, 2020.

[7] D. Forcellini, "A Novel Framework to Assess Soil Structure Interaction (SSI) Effects with Equivalent Fixed-Based Models," *Applied Sciences*, vol. 11, Article ID 10472, 2021.

[8] F. Castelli, S. Grasso, V. Lentini, and M. S. V. Sammito, "Effects of Soil-Foundation-Interaction on the Seismic Response of a Cooling tower by 3D-FEM Analysis," *Geosciences*, vol. 11, p. 200, 2021.

[9] D. Forcellini, "Soil-structure Interaction Analyses of Shallow-Founded Structures on a Potential-Liquefiable Soil deposit," *Soil Dynamics And Earthquake Engineering*, vol. 133, Article ID 106108, 2020.

[10] F. Goktepe, M. Sahin, and E. Celebi, "Small shaking table testing and numerical analysis of free-field site response and soil-structure oscillation under seismic loading," *Bulletin of Engineering Geology and the Environment*, vol. 79, no. 6, pp. 2949–2969, 2020.

[11] S. H. R. Tabatabaiefar, B. Fatahi, and B. Samali, "Numerical and experimental investigations on seismic response of building frames under influence of soil-structure interaction," *Advances in Structural Engineering*, vol. 17, no. 1, pp. 109–130, 2014.

[12] C. Zhu, Z. Chen, and Y. Huang, "Coupled moving particle simulation–finite-element method analysis of fluid–structure interaction in geodisasters," *International Journal of Geomechanics*, vol. 21, no. 6, 2021.

[13] B. Zhang, Y. Huang, and C. Zhu, "Flow–structure interaction mechanism under coriolis conditions," *Journal of Engineering Mechanics*, vol. 147, no. 4, 2021.

[14] Y. Huang, B. Zhang, and C. Zhu, "Computational assessment of baffle performance against rapid granular flows," *Landslides*, vol. 18, pp. 485–501, 2021.

[15] C. Zhu, H. Cheng, Y. Bao, Z. Chen, and Y. Huang, "Shaking table tests on the seismic response of slopes to near-fault ground motion," *Geomechanics and Engineering*, vol. 29, pp. 133–143, 2022.

[16] H. Jahangir and M. Bagheri, "Evaluation of seismic response of concrete structures reinforced by shape memory alloys," *International Journal of Engineering*, vol. 33, pp. 410–418, 2020.

[17] P. Li, S. Liu, Z. Lu, and J. Yang, "Numerical Analysis of a Shaking Table Test on Dynamic Structure-Soil-Structure Interaction under Earthquake Excitations," *Structural Design Of Tall And Special Buildings*, vol. 26, pp. 1–13, 2017.

[18] S. Liu, P. Li, W. Zhang, and Z. Lu, "Experimental Study and Numerical Simulation on Dynamic Soil-Structure Interaction under Earthquake Excitations," *Soil Dynamics And Earthquake Engineering*, vol. 138, Article ID 106333, 2020.

[19] P. Li, J. Yang, and Z. Lu, "Shaking table test and theoretical analysis of the pile–soil–structure interaction at a liquefiable site," *The Structural Design of Tall and Special Buildings*, vol. 27, no. 15, 2018.

[20] J. Yang, P. Li, and Z. Lu, "Large-scale shaking table test on pile-soil-structure interaction on soft soils," *The Structural Design of Tall and Special Buildings*, vol. 28, no. 18, pp. 1–19, 2019.

[21] M. D. Trifunac, M. I. Todorovska, M. I. Manić, and B. D. Bulajic, "Variability of the fixed-base and soil--structure system frequencies of a building—the case of Borik-2 building," *Structural Control and Health Monitoring*, vol. 17, no. 2, pp. 120–151, 2010.

[22] C. Amendola, F. de Silva, A. Vratsikidis, D. Pitilakis, A. Anastasiadis, and F. Silvestri, "Foundation Impedance Functions from Full-Scale Soil-Structure Interaction Tests," *Soil Dynamics And Earthquake Engineering*, vol. 141, Article ID 106523, 2021.

[23] D. Pitilakis, M. Dietz, D. M. Wood, D. Clouteau, and A. Modaressi, "Numerical simulation of dynamic soil-structure interaction in shaking table testing," *Soil Dynamics and Earthquake Engineering*, vol. 28, pp. 453–467, 2008.

[24] K. T. Chau, C. Y. Shen, and X. Guo, "Nonlinear Seismic Soil-Pile-Structure Interactions: Shaking Table Tests and FEM Analyses," *Soil Dynamics And Earthquake Engineering*, vol. 29, pp. 300–310, 2009.

[25] X. Lu, X. Yin, and H. Jiang, "Shaking table scaled model test on a high-rise building with CFT frame and composite core wall," *European Journal of Environmental and Civil Engineering*, vol. 17, no. 8, pp. 616–634, 2013.

[26] SAP, *Integrated Finite Element Analysis and Design of Structures Graphic User Interface Manual*, Computers and Structures, Inc, Berkley, CA, U.S.A, 2000.

[27] F. Goktepe, E. Celebi, A. Jawad, and A. J. Omid, "Numerical and Experimental Study on Scaled Soil-Structure Model for Small Shaking Table Tests," *Soil Dynamics And Earthquake Engineering*, vol. 119, pp. 308–319, 2019.

[28] M. El. Hoseny, J. Ma, and M. Josephine, "Effect of Embedded Basement Stories on Seismic Response of Low-Rise Building Frames Considering SSI via Small Shaking Table Tests," *Sustainability*, vol. 14, p. 1275, 2022.

[29] P. D. Moncarz, *Theory and Application of Experimental Model Analysis in Earthquake Engineering*, stanford university, Stanford, CA, U.S.A, 1981.

[30] W. M. Cheung, X. Qin, N. Chouw, T. Larkin, and R. Orense, "Experimental and Numerical Study of Soil Response in a Laminar Box," in *Proceedings of the 2013 NZSEE Conference*, New Zealand, April 2013.

[31] S. H. R. Tabatabaiefar, *Determining seismic response of mid-rise building frames considering dynamic soil-structure interaction*, PhD Thesis, OPUS, England, U.K, 2012.

[32] Y. Wang, M. Tayyebi, and A. Assari, "Fracture toughness, wear, and microstructure properties of aluminum/titanium/steel multi-laminated composites produced by cross-accumulative roll-bonding process," *Archives of Civil and Mechanical Engineering*, vol. 22, pp. 49–14, 2022.

[33] R. Srinivasan, M. Kamaraj, D. Rajeev, S. Ravi, and N. Senthilkumar, "Plasma Spray Coating of Aluminum–Silicon-MWCNT Blends on Titanium Grade 5 Alloy Substrate for Enhanced Wear and Corrosion Resistance," *Silicon*, vol. 14, 2022.

[34] PEER, *PEER 2010 PEER Strong Motion Database*, University of California, Berkeley, CA, U.S.A, 2010.

[35] R. B. Brinkgreve, *Plaxis 3D*, plaxis bv, Netherland, 2012.

Hindawi
Shock and Vibration
Volume 2022, Article ID 2224198, 9 pages
https://doi.org/10.1155/2022/2224198

*Research Article*

# Study on Response and Influencing Factors of Shield Single/Twin Tunnel under Seismic Loading using FLAC 3D

**Song Li,[1] Yanxiang Chen,[2] Linhua Huang,[1] and Enping Guo[1]**

[1]*School of Civil and Environmental Engineering, Hunan University of Science and Engineering, Yongzhou, Hunan 425199, China*
[2]*College of Civil Engineering and Architecture, Guangxi University, Nanning, Guangxi 530004, China*

Correspondence should be addressed to Linhua Huang; huanglinhua@huse.edu.cn and Enping Guo; guoenping@huse.edu.cn

Received 8 February 2022; Revised 7 March 2022; Accepted 8 March 2022; Published 4 May 2022

Academic Editor: Chongqiang Zhu

Copyright © 2022 Song Li et al. This is an open access article distributed under the Creative Commons Attribution License, which permits unrestricted use, distribution, and reproduction in any medium, provided the original work is properly cited.

The research on the dynamic response and influencing factors of shield tunnel lining under earthquake demonstrates significant engineering value in guiding the design of antiseismic tunnels. In this paper, a nonlinear finite element model of soil-tunnel interaction is established based on FLAC finite difference software, and then Mohr–Coulomb elastoplastic model and dynamic plastic damage model are used to simulate the dynamic characteristics of soil and lining damage of tunnel, and the seismic waves of South Iceland are selected to analyze the residual internal force, dynamic internal force distribution, and the relative deformation of the top and bottom of the arch of the shield tunnel under the earthquake load. Meanwhile, the effects of depth tunnel, lining thickness, and tunnel diameter on the dynamic response of the tunnel are discussed. In addition, the interaction law of horizontal parallel tunnel and the amplification effect on the surface acceleration are also studied. The results show that under the action of a strong earthquake, the bearing capacity of the tunnel decreases sharply, the lining is destroyed, and a large residual internal force appears. When the buried depth of the tunnel is small, the nonlinear effect is more significant, and the $R$ value increases at first and then decreases with the increase in the seismic acceleration. The maximum dynamic bending moment and maximum dynamic axial force of the tunnel lining aggrandize obviously with the increase in tunnel diameter and lining thickness. In particular, the dynamic bending moment has internal force redistribution and deflection under the condition of large tunnel diameter and small lining thickness. Moreover, the interaction of parallel tunnels affects the distribution of internal force and the magnitude of adjacent surface acceleration.

## 1. Introduction

With the rapid development of modern transportation and the accelerated urbanization process, the problem of urban traffic congestion has become increasingly serious. An increasing number of cities have started to build underground transportation structures, such as subway tunnels and cross-river tunnels, among which shield tunnels have been widely used due to their technical and economic superiority.

According to previous research, tunnels and other underground structures have good seismic performance under conventional circumstances and can resist strong earthquake effects, so their seismic design is often neglected. However, with the construction of tunnels in high-intensity regions and changes in their diameters, embedment depths, and other parameters, underground structures such as tunnels can still produce severe damage under strong earthquake effects [1], such as the 2004 Sino-Vietnamese earthquake, when some tunnel linings collapsed in the vault [2], and the 2008 Wenchuan earthquake, when the lining of the Longxi tunnel cavern section produced ruptures in multiple directions [3]. On the other hand, due to the presence of underground structures, which change the nearby surface site conditions, seismic waves produce an amplification effect during transmission, thus affecting the seismic response of adjacent structures underground and at the surface. Numerical simulations and experimental studies have been carried out by a large number of scholars on the causes of seismic damage in tunnels and their influencing [4–6]. Wang and Cai [7] explored the dynamic response law of tunnels at different wavelength ratios by the spectral element method, and the results indicated that the velocity

amplification is proportional to the tunnel diameter, and tunnels with larger diameters are more prone to damage under seismic action. Gao et al. [8] studied the effect of burial depth on the lining stress distribution by shaking table experiments, and the experimental results demonstrated that the lining stress gradually decreases as the tunnel burial depth increases, and the lining seismic response increases significantly when the tunnel burial depth is relatively shallow, whereas the tunnel lining stress shows a gradual convergence when the burial depth reaches 40 m and above. Tao et al. [9] analyzed the dynamic characteristics of tunnels with different burial depths by shaking table tests, and their results showed that the additional bending moment generated by the tunnel structure is inversely proportional to the burial depth, so shallow buried tunnels are more prone to seismic damage compared with deeply buried tunnels. Sederat et al. [10] studied the effect of the contact interface on the elliptical deformation of circular tunnels by using quasi-static numerical analysis to obtain the lining internal forces. Kouretzis et al. [11] carried out a parametric study of shield tunnels to analyze the effect of interfacial friction on the dynamic response of the tunnel lining. Torcato [12] carried out a two-dimensional numerical simulation of the tunnel to study the effects of soil stratification around the tunnel, lining diameter, and liner thickness on the seismic response of the tunnel.

Most of the previous studies were based on shaking table tests. Although shaking table tests have the advantage of being efficient and accurate, the size of the tunnel structure model is limited by the size of the shaking table surface and the model box, and the cost of the experimental study is high. Therefore, it is of great significance to study the effect of tunnel parameters on seismic response through numerical methods. Based on the above research background, numerical models of single and parallel tunnels are developed in this paper using FLAC 3D numerical finite difference software to analyze the effects of burial depth, lining thickness, and lining diameter of a single tunnel on the seismic response of the tunnel, whilst the interaction and ground acceleration amplification effects of parallel tunnels are investigated, thus providing a theoretical reference for the application and promotion of shield tunneling technology.

## 2. Numerical Analysis

*2.1. Numerical Model and Validation.* In this paper, the numerical model is established by using FLAC 3D general finite element [13]. In order to simulate the infinite foundation conditions, the model is selected to eliminate the influence of the boundary with a larger calculation area, the model calculation domain is 180 m long and 70 m high, Figure 1 shows the grid division of the tunnel model calculation domain, the grid is gradually encrypted from the outside to the inside of the tunnel, and the grid size is based on the principle that the seismic force-frequency can be transmitted within 10 Hz [14].

To reduce the influence of seismic wave reflection at the soil subinterface and to simplify the study, the same parameters are used for all soil bodies in this paper. The dynamic response of the lining is simulated using elastic beam units, and complete bonding is assumed between the soil and the tunnel without relative slip and separation. The cumulative damage to the lining under the action of seismic forces is considered through a dynamic plastic damage model, and the calculated mechanical parameters of the tunnel and soil are shown in Table 1.

The seismic analysis of the tunnel is divided into two steps; first, the model is analyzed statically, accounting for the gravitational effect of the structure, and subsequently the dynamic analysis is performed by inputting the seismic force-time interval through the bottom of the model. The seismic loads were loaded using the 2000 South Iceland seismic acceleration timescale, and the seismic acceleration versus time curve and its power spectrum are shown in Figure 2.

Figure 3 shows the distribution of bending moment and axial force at each position of the liner under the action of seismic force. From the figure, it can be seen that the bending moment and axial force are unevenly distributed, and there are extreme value points for both bending moment and axial force at the diagonal position of positive and negative 45° of the liner, and the dynamic bending moment has the maximum value at 45°, and the dynamic axial force has the maximum value near 315°. The values of the dynamic bending moment are relatively large, while the values of dynamic axial force are relatively small. During the calculation, the soil near the tunnel is deformed, which leads to the weakening of the lining circumferential restraint effect, so when the soil deformation increases further, the dynamic bending moment also increases gradually.

Figure 4 shows the time course of bending moment and axial force of the liner at 45° position under the seismic force. From the figure, it can be seen that the time course of liner bending moment and axial force have a similar distribution pattern with the time course of seismic acceleration, and the curve of liner bending moment and axial force also fluctuates greatly near 10 s due to the sudden change of seismic acceleration. The permanent residual load of the liner was generated after the end of the applied seismic load, mainly due to the partial damage of the liner under the seismic force, which caused the reduction of the bearing capacity and made the residual internal force significant, and the residual bending moment was about 60% of the maximum moment, and the residual axial force load was about 30% of the maximum value. The residual internal force of the lining still maintains a large value after the seismic load, so the effect of residual internal force cannot be neglected when calculating the seismic response of this type.

*2.2. Effect of Burial Depth on Seismic Response.* According to available data, the geometric parameters of the tunnel have an important influence on the seismic dynamic response of the tunnel structure. Previous studies are usually carried out using shaking table tests, but some of the parameters cannot be accurately simulated due to the size effect, so it is important to use numerical methods to study the influence of tunnel parameters on the seismic response. Based on the

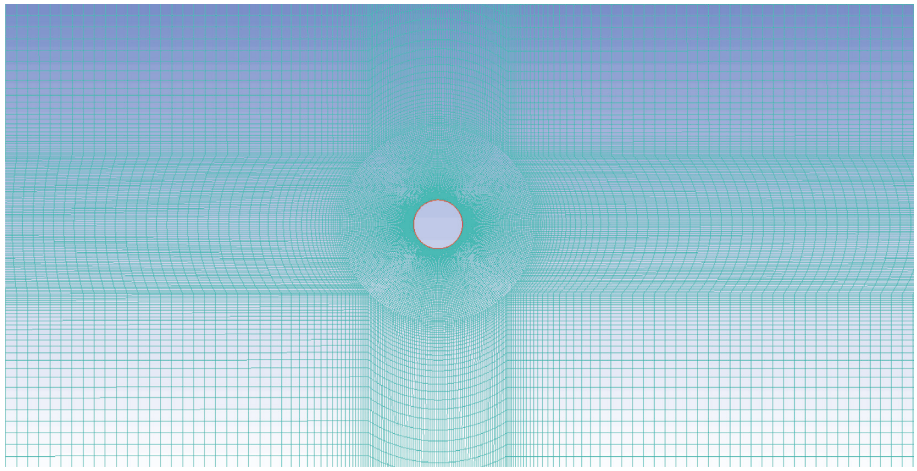

Figure 1: Model mesh of tunnel-soil.

Table 1: Parameters of tunnel and soil.

| Tunnel parameters | | Soil parameters | |
|---|---|---|---|
| Burial depth (m) | 50 | Density (kg/m$^3$) | 2000 |
| Diameter (m) | 10 | Shear wave speed (m/s) | 300 |
| Thickness (m) | 0.5 | Friction angle (°) | 23 |
| Density (kg/m$^3$) | 2500 | Bonding force (MPa) | 0.03 |
| Modulus of elasticity (MPa) | 24.8 | Poisson's ratio | 0.3 |
| Poisson's ratio | 0.2 | Damping ratio (%) | 5 |

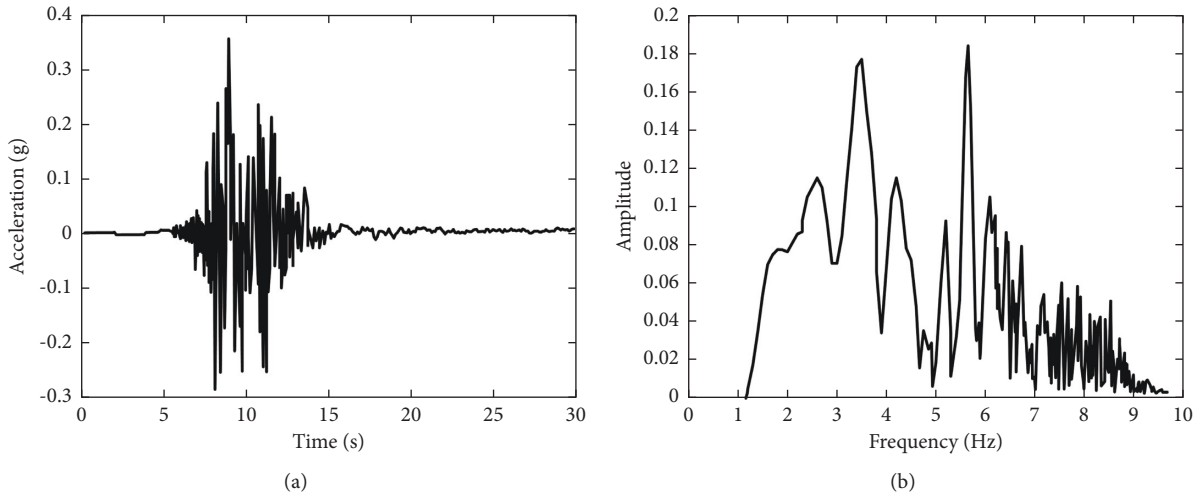


Figure 2: (a) Acceleration time history of South Iceland earthquake. (b) Power spectrum of South Iceland earthquake.

aforementioned model, this paper analyzes the effects of three parameters on the seismic response of shield tunnels by establishing tunnel models with different lining burial depths, lining thicknesses, and lining diameters.

Figure 5 shows the changes of dynamic bending moment and dynamic axial force response of the liner with different tunnel burial depths. It can be seen from the figure that the dynamic bending moment and dynamic axial force both increase with the increase in burial depth, and the distribution law of dynamic axial force is basically the same for each condition, while the distribution law of dynamic bending moment is relatively complicated. When the burial depth is shallow, the maximum dynamic bending moment of the lining appears at the right arch shoulder and left arch corner position, and with the increase in the burial depth, the dynamic bending moment fluctuates significantly along the axial direction, which may be caused by the reflection of seismic waves in the bottom area of the tunnel. The dynamic axial force shows a strong distribution pattern, and the maximum dynamic axial force at different burial depths appears near the diagonal of plus or minus 45°.

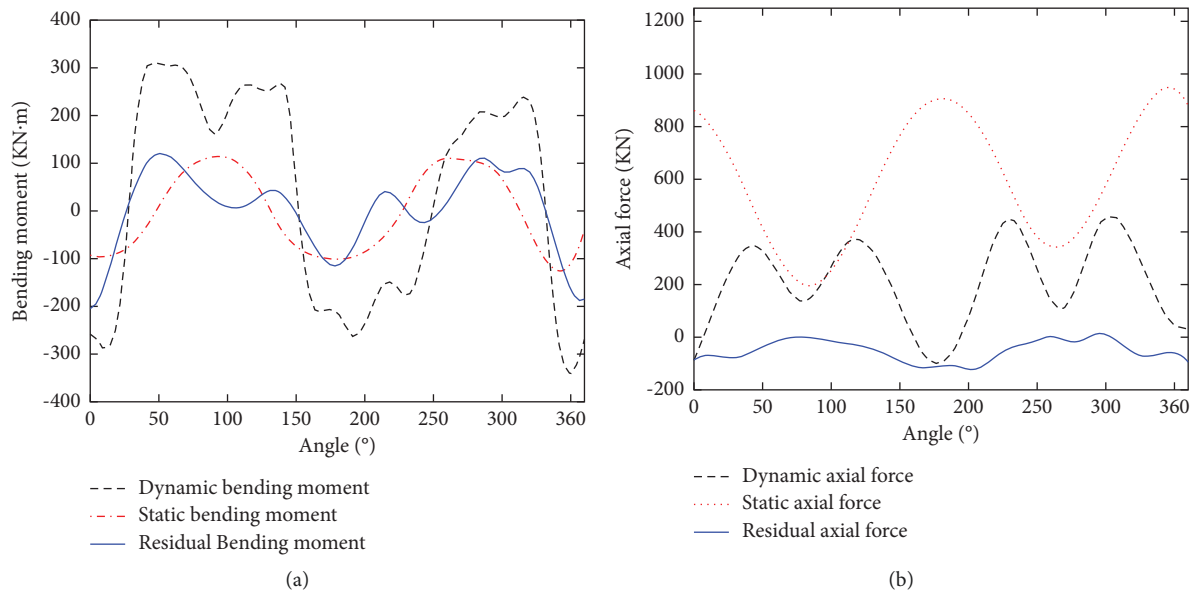


Figure 3: (a) Distribution of bending moment at each position of lining under seismic force. (b) Distribution of axial force at each position of lining under seismic force.

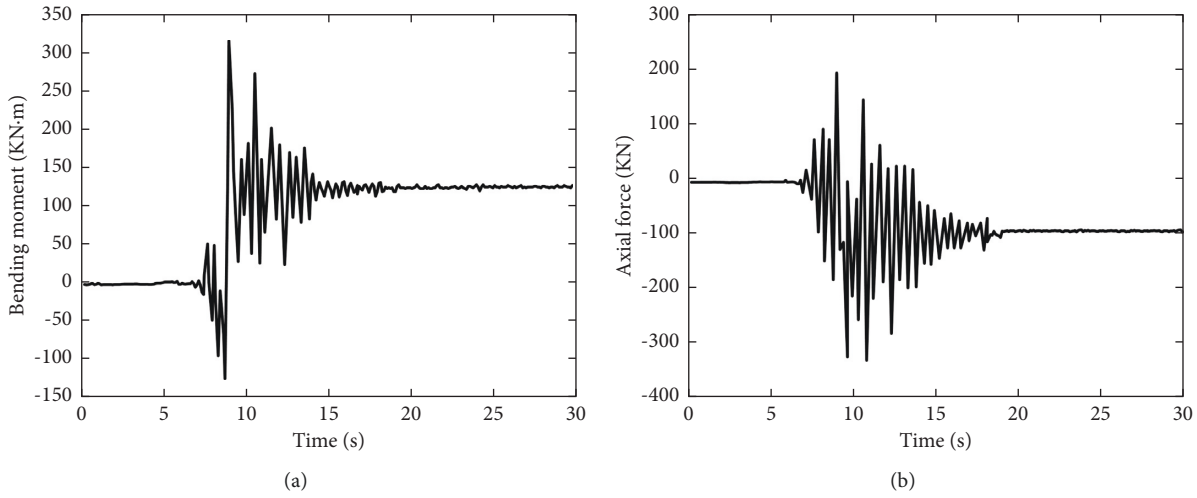


Figure 4: (a) Time history of bending moment of 45° position under seismic force. (b) Time history of axial force of lining of 45° position under seismic force.

Figure 6 shows the changes of relative displacement and $R$ value of liner arch bottom with seismic intensity and tunnel burial depth; $R$ value represents the ratio of relative displacement of the arch bottom to free field displacement at the same position. At the same time, the displacement of the arch top base under different burial depths is different, and the relative displacement of the arch top base is the largest when the burial depth is 35 m. With the change of seismic load acceleration, when the buried depth is large, the $R$ value increases with the increase of seismic load intensity. When the burial depth is small, the $R$ value increases first with the seismic acceleration and then decreases, and the maximum value of $R$ value exists near the acceleration of 0.2 g. When the seismic load acceleration continues to increase, the $R$ value decreases significantly. The main reason for this is that the Mohr–Coulomb principal model is used for the soil properties, and there is an amplification of the acceleration in the soil layer [15]. In addition, when the acceleration is less than 0.2 g and the burial depth is large, the calculated $R$ value is basically around 1.0, indicating that when the tunnel is buried at a large depth, the nonlinear effect of the soil is small, and it is reasonable to use the free field method for seismic calculations.

*2.3. Effect of Liner Thickness on Seismic Response.* Figure 7 shows the maximum dynamic bending moment and dynamic axial force at each position under different lining thicknesses, the calculated burial depth is 12 m, and the peak ground vibration acceleration is 0.2 g. It is seen from the figure that the

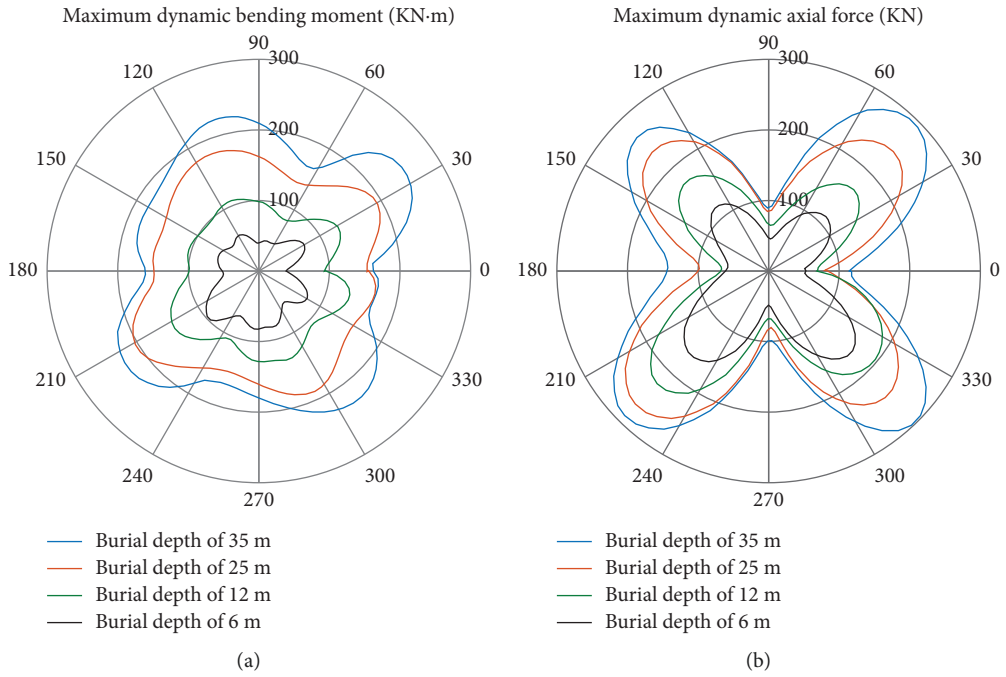


Figure 5: (a) Maximum dynamic bending moment of lining at different positions under different embedded depths. (b) Maximum dynamic axial force of lining at different positions under different embedded depths.

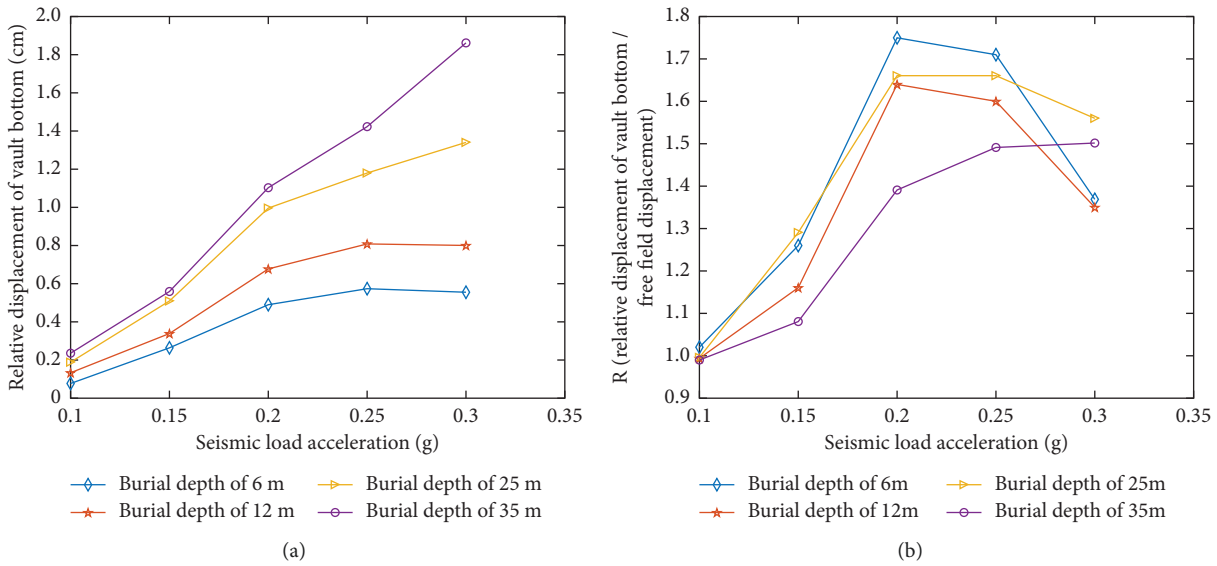


Figure 6: (a) Relative displacement of vault and bottom under different embedded tunnel depths. (b) Distribution of $R$ value under different embedded tunnel depths.

larger the lining thickness is, the values of dynamic bending moment and dynamic axial force of the lining also increase. The distribution law of dynamic bending moment changed with the thickness, and an obvious deflection phenomenon occurred, while the distribution law of dynamic axial force did not change significantly with the thickness change. When the lining thickness is small, there are maximum dynamic bending moments at four positions of the lining 0°, 90°, 180°, and 270°, which mainly cause the redistribution of the internal forces in the lining and change the force characteristics of the tunnel [16, 17]. The distribution pattern of dynamic axial force is less affected by the lining thickness, and the maximum dynamic axial force for each condition occurs near 225° and 315° of the tunnel, and the dynamic axial force amplitude does not change significantly with the increase in lining thickness.

*2.4. Effect of Liner Diameter on Seismic Response.* Figure 8 shows the effect of different tunnel diameters on the dynamic bending moment and dynamic axial force under

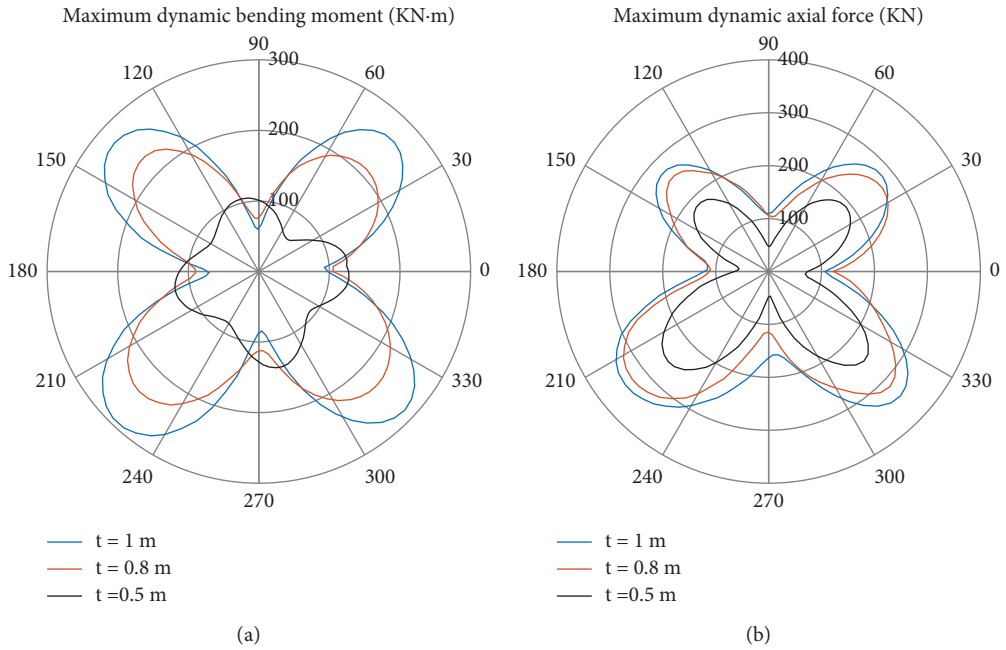


Figure 7: (a) Maximum dynamic bending moment at different positions under different lining thicknesses. (b) Maximum dynamic axial force at different positions under different lining thicknesses.

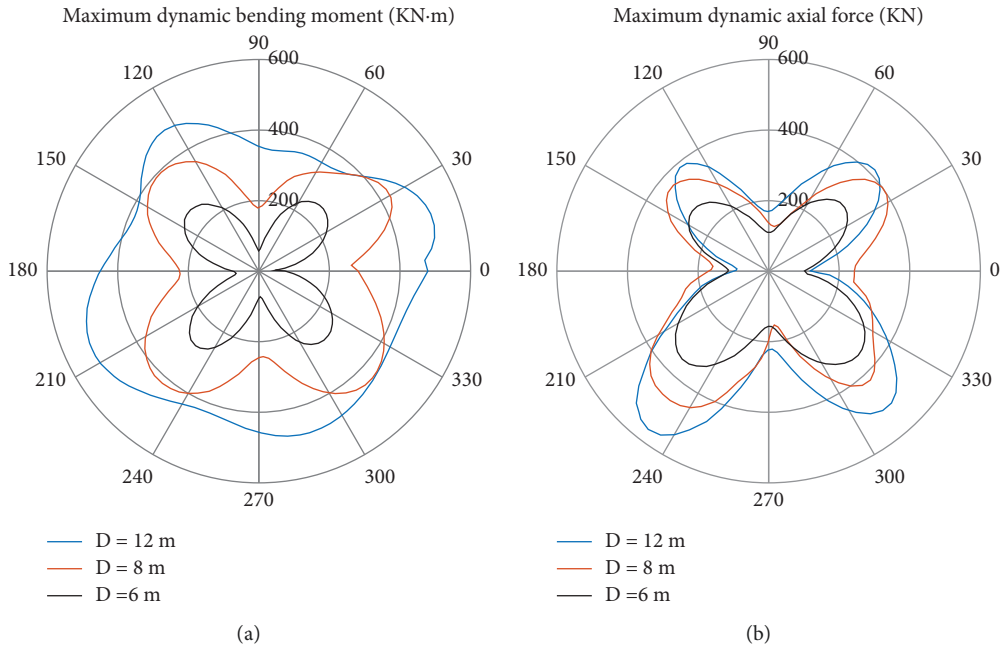


Figure 8: (a) Maximum dynamic bending moment at different positions under different lining diameters. (b) Maximum dynamic axial force at different positions under different lining diameters.

seismic forces. It can be seen from the figure that the maximum dynamic moment and the maximum dynamic axial force of the tunnel structure both increase with the diameter of the tunnel under the same seismic load, and the dynamic axial force of the lining is less affected by the diameter than the dynamic moment. When the tunnel diameter is small, the maximum dynamic bending moment is distributed at plus or minus 45°, and when the tunnel diameter is large, the dynamic bending moment distribution law becomes complex and irregular, so for large diameter shallow buried tunnel, the mechanical model simply assumes that the tunnel structure is subject to the action of far-field shear deformation and is not reasonable. The maximum dynamic axial force of the liner increases gradually with the diameter, and the change of tunnel diameter has a greater effect on the dynamic axial force at the liner arch angle

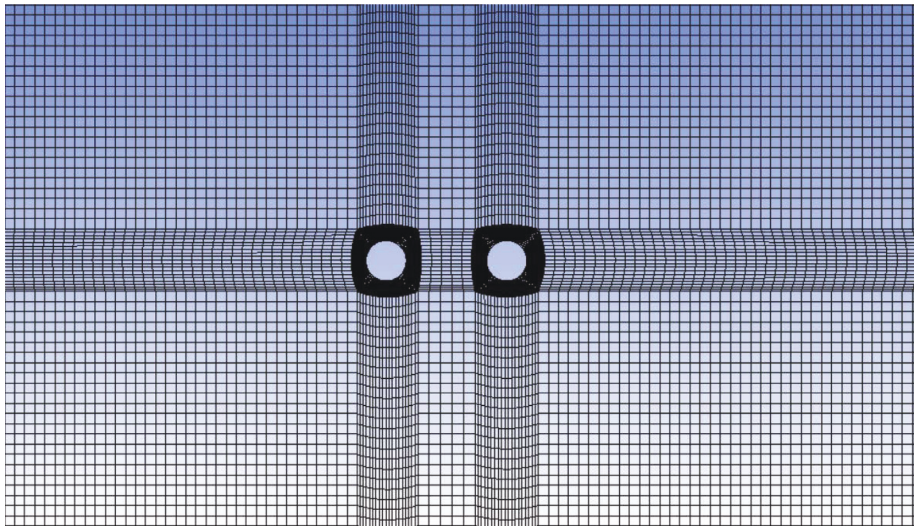

Figure 9: Model of parallel twin-tunnel and soil.

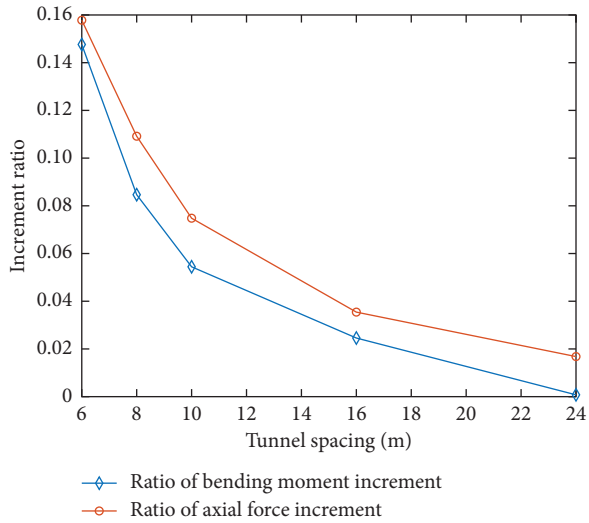


Figure 10: Ratio of internal force increment varies with spacing.

position, while the dynamic axial force at other positions is less affected by the change of diameter.

*2.5. Interaction and Amplification of Parallel Tunnels under Seismic Effects.* Most of the currently built shield tunnels are parallel double-row tunnels, which are more complex due to the reflection of seismic waves, and the loads on the tunnels may be significantly different compared with the single tunnel case, so it is necessary to carry out a study on the interaction effects of parallel tunnels under seismic effects [18, 19]. Based on the aforementioned study, a parallel twin-tunnel model is developed in this paper, as shown in Figure 9. The peak seismic acceleration is 0.2 g, the tunnel radius is 8 m, the lining thickness is 0.5 m, and the burial depth is 12 m, and the seismic response is calculated for five different tunnel center distances of 6 m, 8 m, 10 m, 16 m, and 24 m, respectively.

Figure 10 shows the variation of the incremental force in parallel tunnels compared with the tunnel spacing, where the incremental ratio is defined as (maximum internal force in a parallel tunnel – maximum internal force in a single tunnel)/maximum internal force in a single tunnel. As can be seen from Figure 10, with the increase in tunnel spacing, the incremental ratio of tunnel internal force gradually decreases, and the bending moment is affected more obviously compared with the axial force. When the spacing of parallel tunnels is 6 m, the incremental ratio of bending moment is about 16% and the incremental ratio of axial force is about 15%. When the spacing of tunnels is greater than 1.25 times of tunnel diameter, parallel tunnels have less influence on each other and the incremental ratio of tunnel bending moment and axial force gradually converge, and their values are less than 5%.

Under seismic loading, the presence of underground tunnels amplifies the surface shaking, and the incident waves

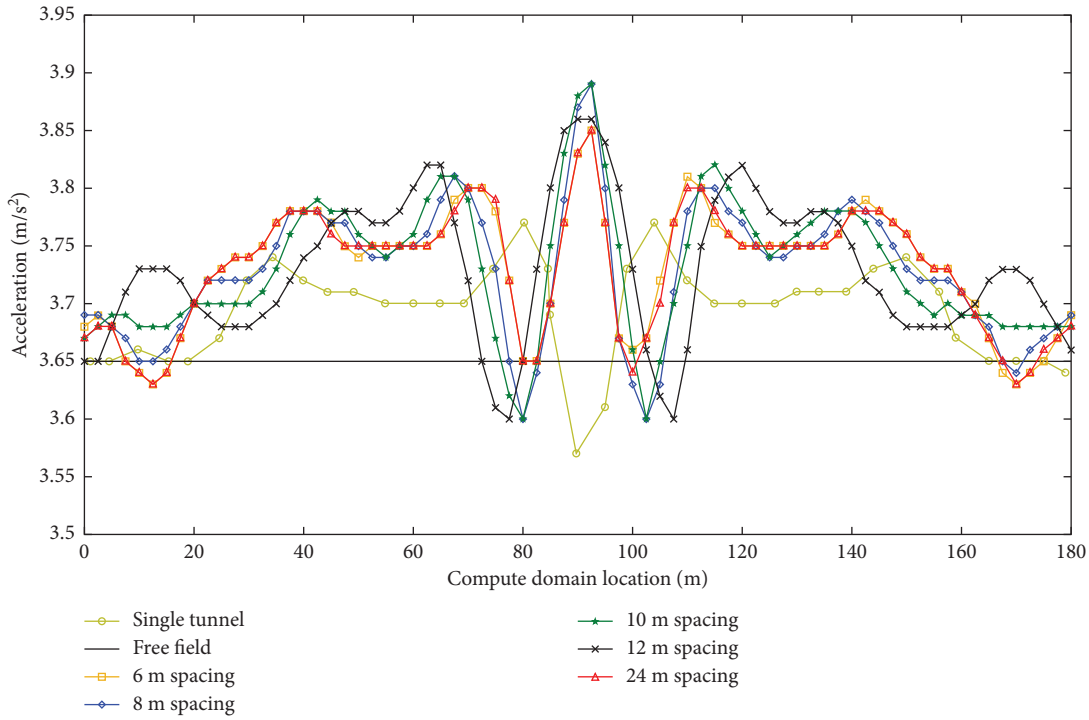


Figure 11: Comparison of peak ground acceleration.

interacting between parallel tunnels amplify this effect [20]. The amplification effect of parallel tunnels with different spacing was compared by monitoring the acceleration at the surface at the top of the computational domain. As seen in Figure 11, (1) in the single tunnel condition, the acceleration at the center of the tunnel is smaller than the free field acceleration, which is mainly due to the reflection effect at the tunnel location during the upward transmission of seismic waves, reducing the ground acceleration, while the acceleration at both sides of the tunnel increases significantly, and its maximum value increases by 3.4% compared with the free field acceleration; (2) for parallel tunnels, the acceleration directly above the tunnel is basically the same as the free field acceleration under seismic loading, and the seismic acceleration has a maximum value in the middle of the two parallel tunnels, which is 6.35% higher than the free field acceleration. The maximum accelerations calculated for parallel tunnels with different spacing are greater than the single tunnel condition, so the interaction of parallel tunnels cannot be neglected.

## 3. Conclusions

In this paper, a nonlinear finite element model of soil-tunnel interaction is established with a shield tunnel as the research object, and the South Iceland seismic wave curve is used to study the geometric parameters on the dynamic response of the tunnel and the interaction of parallel tunnels under the action of seismic loads, and the following conclusions are obtained through the analysis:

(1) The time course curves of bending moment and axial force of the lining under the action of seismic force coincide with the distribution pattern of South Iceland seismic acceleration time course curve, and the maximum values of bending moment and axial force appear near 10 s. The lining is damaged by the seismic force, and the bearing capacity is reduced. After the seismic load is loaded, the lining has a large residual internal force, and the residual bending moment is about 60% of the maximum bending moment and the residual axial force is about 30% of the maximum axial force.

(2) For different tunnel embedment depths, the maximum value of dynamic bending moment is at the right arch shoulder and left arch angle of the tunnel, and the maximum value of dynamic axial force appears near the plus or minus 45° diagonal. When the burial depth is larger, the $R$ value increases with the increase in seismic load intensity. When the burial depth is smaller, the nonlinear effect is more significant, and the $R$ value shows a trend of increasing and then decreasing with the increase in seismic load acceleration.

(3) Under the same seismic load, the maximum dynamic bending moment and maximum dynamic axial force of tunnel lining increase with the increase in tunnel diameter and lining thickness, the influence of tunnel diameter and lining thickness on dynamic axial force is smaller than that of the dynamic bending moment, the distribution of dynamic axial force under each condition is similar, and the maximum value appears around 225° and 315°. Moreover, due to inertia and plastic deformation of soil, the dynamic moments

are redistributed and deflected at larger tunnel diameters and smaller lining thicknesses.

(4) The interaction of the parallel tunnels affects their internal force distribution, which increases significantly when the spacing between the parallel tunnels is small compared with the single tunnel case. On the other hand, the presence of tunnels causes the incident waves and the reflected waves between the tunnels to superimpose on each other thus amplifying the ground acceleration, and the peak increment of ground acceleration in the middle of the parallel tunnel is doubled compared with the single tunnel case.

## Data Availability

The data supporting the results of this study are obtained upon request to the corresponding author.

## Conflicts of Interest

The authors declare that they have no conflicts of interest regarding the publication of this paper.

## References


[1] X. Fan, G. Scaringi, O. Korup et al., "Earthquake-Induced cghpmi," *Reviews of Geophysics*, vol. 57, no. 2, pp. 421–503, 2019.

[2] H. Yu, J. Chen, A. Bobet, and Y. Yuan, "Damage observation and assessment of the Longxi tunnel during the Wenchuan earthquake," *Tunnelling and Underground Space Technology*, vol. 54, pp. 102–116, 2016.

[3] T. Li, "Failure characteristics and influence factor analysis of mountain tunnels at epicenter zones of great wenchuan earthquake," *Journal of Engineering Geology*, vol. 16, no. 6, pp. 742–750, 2008.

[4] B. Aicha, S. Mezhoud, B. Tayeb, K. Toufik, and N. Abdelkader, "Parametric study of shallow tunnel under seismic conditions for constantine motorway tunnel, Algeria," *Geotechnical & Geological Engineering*, vol. 2022, pp. 1–12, 2022.

[5] J. Wang, Y. Hu, B. Fu, H. Shan, H. Wei, and G. Cui, "Study on antiseismic effect of different thicknesses of shock absorption layer on urban shallow buried double arch rectangular tunnel," *Shock and Vibration*, vol. 2022, Article ID 4863756, 9 pages, 2022.

[6] W. Sun, Q. Ma, C. Yang et al., "Mesenchymal scealimprcem," *Immunological Investigations*, vol. 2022, pp. 1–19, 2022.

[7] X. Wang and M. Cai, "Influence of wavelength-to-excavation span ratio on ground around deep underground excavations," *Tunnelling and Underground Space Technology*, vol. 49, pp. 438–453, 2015.

[8] F. Gao, C. Sun, X. Tan, Z. Yi, and L. Hu, "Seismic response shaking table test of different buried tunnels," *Rock and Soil Mechanics*, vol. 36, no. 9, pp. 2517–2523, 2015.

[9] L. Tao, X. Qi, S. Li, H. Sen, and A. Linxuan, "Seismic dynamic response of mountain tunnel with different depth is studied by shaking table test," *Engineering seismic and reinforcement transformation*, vol. 37, no. 6, pp. 1–7, 2015.

[10] H. Sedarat, A. Kozak, Y. M. A. Hashash, A. Shamsabadi, and A. Krimotat, "Contact interface in seismic analysis of circular tunnels," *Tunnelling and Underground Space Technology*, vol. 24, no. 4, pp. 482–490, 2009.

[11] G. P. Kouretzis, S. W. Sloan, and J. P. Carter, "Effect of interface friction on tunnel liner internal forces due to seismic S- and P-wave propagation," *Soil Dynamics and Earthquake Engineering*, vol. 46, pp. 41–51, 2013.

[12] D. M. M. F. Torcato, *Seismic Behaviour of Shallow Tunnels in Stratified ground*, Univeridade Ténica de Lisboa, Lisbon, Portugal, 2010.

[13] M. Bonini, M. Barla, and G. Barla, "FLAC applications to the analysis of swelling behavior in tunnels," *FLAC and Numerical Modeling in Geomechanics*, pp. 329–333, CRC Press, Boca Raton, FL, USA, 2020.

[14] H. Li, J. Wu, J. Liu, and L. Yubing, "Finite element mesh generation and decision criteria of mesh quality," *China Mechanical Engineering*, vol. 23, no. 3, pp. 368–377, 2012.

[15] D. Fu and Y. Gu, "Research onseismic response of mountain tunnel considering soil-structure dynamic interaction," *Journal of Guangxi University(Natural Science Edition)*, vol. 44, no. 1, pp. 176–182, 2019.

[16] R. C. Gomes, "Effect of stress disturbance induced by construction on the seismic response of shallow bored tunnels," *Computers and Geotechnics*, vol. 49, pp. 338–351, 2013.

[17] Z. Zhang, B. Chen, H. Li, and H. Zhang, "The performance of mechanical characteristics and failure mode for tunnel concrete lining structure in water-rich layer," *Tunnelling and Underground Space Technology*, vol. 121, Article ID 104335, 2022.

[18] X. Jiang, W. Liu, H. Yang, J. Zhang, and L. Yu, "Study on dynamic response characteristics of slope with double-arch tunnel under seismic action," *Geotechnical & Geological Engineering*, vol. 39, no. 2, pp. 1349–1363, 2021.

[19] L. Pai and H. Wu, "Multi-attribute seismic data spectrum analysis of tunnel orthogonal underpass landslide shaking table test," *Soil Dynamics and Earthquake Engineering*, vol. 150, Article ID 106889, 2021.

[20] China Planning Press, *Gb 50909-2014, Code for Seismic Design of Urban Rail Transit Structures: GB 50909-2014*, China Planning Press, Beijing, China, 2014.